UC San Diego
UC San Diego Electronic Theses and Dissertations

Title
Materials Passivation and Synthesis Using Atomic Layer Deposition-based Techniques

Permalink
https://escholarship.org/uc/item/4fq515qx

Author
Ueda, Scott Toshio

Publication Date
2021

Peer reviewed|Thesis/dissertation

eScholarship.org Powered by the California Digital Library
University of California

UNIVERSITY OF CALIFORNIA SAN DIEGO

Materials Passivation and Synthesis Using Atomic Layer Deposition-Based Techniques

A dissertation submitted in partial satisfaction of the requirements for the degree Doctor of Philosophy

in

Materials Science and Engineering

by

Scott Toshio Ueda

Committee in Charge:

Professor Andrew C. Kummel, Chair
Professor Prabhakar Rao Bandaru
Professor David Fenning
Professor Eric Fullerton
Professor Yu-Hwa Lo
Professor Ying Shirley Meng

2021

Copyright

Scott Toshio Ueda, 2021

All Rights Reserved

The Dissertation of Scott Toshio Ueda is approved, and it is acceptable in quality and form for publication on microfilm and electronically.

University of California San Diego

2021

DEDICATION

To my mother, Linda, and father, Martin. It was only through your steadfast encouragement and support that this was possible.

EPIGRAPH

When an old and distinguished person speaks to you, listen to him carefully and with respect — but do not believe him. Never put your trust into anything but your own intellect. Your elder, no matter whether he has gray hair or has lost his hair, no matter whether he is a Nobel laureate — may be wrong. The world progresses, year by year, century by century, as the members of the younger generation find out what was wrong among the things that their elders said. So you must always be skeptical — always think for yourself.

Linus Pauling

TABLE OF CONTENTS

Dissertation Appoval Page....................iii

Dedication....................iv

Epigraph....................v

Table of Contents....................vi

List of Symbols and Abbreviations....................x

List of Figures....................xiii

Acknowledgments....................xv

Vita....................xviii

Abstract of the Dissertation....................xx

Chapter 1....................1
Introduction

1.1 Scaling of Microelectronic Circuits....................1

1.2 Fundamentals of Atomic Layer Deposition....................2

1.3 Multi Chamber Vacuum System....................3

1.4 Scanning Tunneling Microscopy....................4

1.5 Scanning Tunneling Spectroscopy....................5

1.6 X-ray Photoelectron Spectroscopy....................6

1.7 References....................11

Chapter 2....................13
Electronic Passivation of PbSe Quantum Dot Solids by Trimethylaluminum Vapor Dosing

2.1 Abstract....................13

2.2 Introduction..13

2.3 Experimental..15

2.3.1 Materials..15

2.3.2 Quantum Dot Synthesis..15

2.3.3 Basic Characterization..16

2.3.4 Scanning tunneling Microscopy..17

2.3.5 X-ray Photoelectron Spectroscopy..17

2.3.6 Field Effect Transistor Measurements 18

2.4 Results and Discussion..19

2.4.1 Basic quantum dot film characterization..19

2.4.2 STM measurements of QD film before and after TMA dosing.........................20

2.4.3 STS measurements of QD film before and after TMA dosing.........................21

2.4.4 XPS study of QD surface oxidation...22

2.4.5 Thermodynamic analysis of TMA reaction with trace oxides on PbSe 23

2.4.6 Field Effect Transistor Measurements...24

2.5 Conclusions..26

2.6 Acknowledgements..26

2.7 References..34

Chapter 3.. 40
Tris(dimethylamido)aluminum(III) and N_2H_4: Ideal precursors for the deposition of large grain, oriented c-axis AlN on Si via atomic layer annealing

3.1 Abstract..40

3.2 Introduction..40

3.3 Experimental..42

3.3.1 Materials……………………………………………………………….……………..42

3.3.2 Sample Preparation……………………………………………………….………..43

3.3.3 AlN Deposition……………………………………………………..………...43

3.3.4 X-ray Photoelectron Spectroscopy (XPS) ……………………………….……….44

3.3.5 Structural Analysis……………………………………………….…………….……..44

3.4 Results and Discussion..45

3.4.1 Comparison of TMA and TDMAA at 225 °C..45

3.4.2 Structural Analysis of Films Deposited at 225 °C..46

3.4.3 Comparison of TMA and TDMAA at 400 °C..46

3.4.4 Structural Analysis of Films Deposited at 400 °C..48

3.4.5 Templated Growth of Sputtered AlN...48

3.5 Conclusions...49

3.6 Acknowledgments...50

3.7 References...59

Chapter 4..64
Experimental and Theoretical Determination of the Role of Ions in Atomic Layer Annealing

4.1 Abstract...64

4.2 Introduction...64

4.3 Experimental...66

4.3.1 Materials……………………………………………………………….……………..66

4.3.2 Sample Preparation……………………………………………………….………..66

4.3.3 AlN Deposition……………………………………………………..………...66

4.3.4 X-ray Photoelectron Spectroscopy (XPS) ……………………………….……….67

4.3.5 X-ray Difrraction……………………..……………………………….…………….……..68

4.3.6 Atomic Force Microscopy…………………………………………………….….……..68

4.4 Results and Discussion...68

4.4.1 Effect of Inert Ion Mass on Atomic Layer Annealing………………….…………68

4.4.2 Effect of Plasma Delay Time on Atomic Layer Annealing………………………..70

4.4.3 Effect of Intermittent Atomic Layer Annealing …………………………………...71

4.4.4 Molecular Dynamics Simulations..72

4.5 Conclusions...74

4.6 Acknowledgements..75

4.7 References..84

LIST OF SYMBOLS AND ABBREVIATIONS

Å	angstrom
AFM	atomic force microscopy
ALA	atomic layer annealing
ALD	atomic layer deposition
At. %	atomic percentage
BE	binding energy
BEOL	back end of line
CBM	conduction band minimum
CVD	chemical vapor deposition
°C	degrees Celsius
DC	direct current
E_F	Fermi level
E_g	band gap
E_i	intrinsic Fermi level
eV	electron volt
Eq.	equation
FET	field effect transistor
FWHM	full width at half maximum
GIXRD	grazing-incidence x-ray diffraction
HF	hydrofluoric acid
HOPG	highly ordered pyrolytic graphite
I	electric current

K	kelvin
KE	kinetic energy
L	Langmuir
LDOS	local density of states
LJ	Lennard-Jones
MD	molecular dynamics
nA	nanoampere
nm	nanometer
PEALD	plasma enhanced atomic layer deposition
PVD	physical vapor deposition
ps	picosecond
QD	quantum dot
R_q	root mean square roughness
RF	radio frequency
SAXS	small angle x-ray scattering
SEM	scanning electron microscopy
SL	superlattice
SPM	scanning probe microscopy
SRC	Semiconductor Research Corporation
STM	scanning tunneling microscopy
STS	scanning tunneling spectroscopy
TDMAA	tris(dimethylamido) aluminum
TEM	transmission electron microscopy

TMA	trimethylaluminum
UHV	ultra high vacuum
V	volts
VBM	valence band maximum
W	watt
XPS	x-ray photoelectron spectroscopy
XRD	x-ray diffraction
XRR	x-ray reflectivity

LIST OF FIGURES

Figure 1.1 Schematic diagram of a prototypical ALD process...8

Figure 1.2 Schematic diagram of the multi-chamber vacuum system……………………9

Figure 1.3 Schematic diagram a typical STM imaging circuit..10

Figure 2.1 The PbSe QD epitaxial superlattices studied by STM……………………….28

Figure 2.2 Effect of TMA dosing on STM image quality……………………………….29

Figure 2.3 Effect of TMA dosing on QD band gap……………………………………...30

Figure 2.4 Figure 4. Effect of TMA dosing on the Fermi level of QDs in the first and second QD monolayers……………………………………………………………………..31

Figure 2.5 XP spectra before and after TMA dosing…………………………………….32

Figure 2.6 Impact of TMA dosing on charge transport in QD field-effect transistors…..33

Figure 3.1 Schematic Diagram of ALA AlN……………………………………………..51

Figure 3.2 XPS Chemical Composition Data for both Thermal and ALA Processes using TMA and TDMAA at 225 °C…………………………………………………………….52

Figure 3.3 XRD Data for both Thermal and ALA Processes using TMA and TDMAA at 225 °C…………………………………………………………………………………….53

Figure 3.4 XPS Chemical Composition Data for both Thermal and ALA Processes using TMA and TDMAA at 400 °C…………………………………………………………..…54

Figure 3.5 XRD Data for both Thermal and ALA Processes using TMA and TDMAA at 400 °C…………………………………………………………………………………….55

Figure 3.6 Bright Field TEM Image of a 10 nm ALA AlN layer………………………....56

Figure 3.7 XRD data comparing AlN films using a 25 nm amorphous AlN buffer layer with a 25 nm ALA AlN buffer layer……………………………………………………..57

Figure 3.8 Bright Field TEM Image of a 25 nm ALA AlN templating the growth of 290 nm sputtered AlN………………………………………………………………………...58

Figure 4.1 Schematic Diagram of the ALA AlN Process……………………………...76

Figure 4.2 GIXRD data comparing ALA AlN films using Ne, Ar, or Kr gas at various bias voltages……………………………………………………………………………..77

Figure 4.3 AFM data comparing effect inert gas used during ALA……………………..78

Figure 4.4 GIXRD and XPS comparing effect of ALA delay time on crystallinity...…...79

Figure 4.5 GIXRD data comparing effect of cycles per ALA treatment………………...80

Figure 4.6 Schematic diagram of ion impact simulation………………………………...81

Figure 4.7 Simulation results during initial contact phase of ion collision……………...82

Figure 4.8 MD simulation of the local structure relaxation of AlN with an impinging atom………………………………………………………………………………………83

ACKNOWLEDGEMENTS

First and foremost, I would like to acknowledge my advisor, Professor Andrew Kummel, who has been an extremely supportive and dedicated mentor throughout my years in the lab. From my first day to my last, I have continued to learn and have grown as both a scientist and a scholar. From day one, you were there for guidance no matter what time of day or night and for that, I thank you.

I would also like to acknowledge Dr. Kasra Sardashti who was a great senior student and an even better friend. I will never forget those sleepless nights performing experiements and analyzing data. You are truly one of the hardest working, smartest, and kindest people I know and I am looking forward to the great research that I know will emerge from your lab. To Dr. Steven Wolf, I will never forget your guidance for my first foray into vacuum science. You taught me everything I needed to know to get my research career started and I will not soon forget our adventures in lab, at conference, or on personal travel. To Dr. Iljo Kwak, thank you for your patience and guidance in in STM/STS, you were a great mentor and one of the kindest and most easy going people I know. To Jong and Chris, your antics and advice made my time in graduate school go much more quickly and smoothly—I hope that one day your songs become a smash hit. And to Dr. Fruhberger and the rest of the Nano3 cleanroom staff, thank you allowing me my first opportunity in the semiconductor field.

I must also acknowledge the numerous group members and collaborators with whom I have had the pleasure of working with the past few years: Aaron McLeod, Mike Breeden, Yunil Cho, James Huang, Victor Wang, Harshil Kashyap, Jimmy Kuo, Alex

Abelson, and Caroline Qian. You are all amazing scholars and will undoubtably accomplish much in whatever pursuits you eventually choose to go into.

A special thanks to our partners in industry such as Applied Materials, Rasirc, EMD, and Raytheon for not only providing financial support but also for providing invaluable technical expertise. Kartik from Applied provided immense help on RF engineering, Dan from Rasirc provided a huge amount of help setting up peroxide and hydrazine sources, Ravi, Jacob and Dan provided so much help with Al precursor chemistry, and Jay, Marty, and Jeff provided much needed expertise on SiC substrates as well as industrial applications to this project. .

Thanks also to committee members for participating in my senate and thesis defense presentations. My committee includes Professor Prabhakar Bandaru, Professor David Fenning, Professor Eric Fullerton, Professor Yu-Hwa Lo, and Professor Shirley Meng.

Last, but not least, I would like to thank my family who have continually supported me throughout my graduate journey. To my parents Martin and Linda, you gave me everything I needed to succeed in life and I will always be grateful. And to my grandmother, although you could not see me graduate, I know you would be proud of what I have accomplished.

This work was funded in part through the UC Office of the President, Applied Materials, Rasirc, and the Semiconductor Research Corporation (including such constituent member companies as EMD Electronics, Raytheon Technologies, and TSMC).

Chapter 2, in part or in full, is a reprint of the material as it appears in Applied Surface Science. S. T. Ueda, I. Kwak, A. Abelson, S. Wolf, C. Qian, M. Law, and A. C.

Kummel, ”Electronic Passivation of PbSe Quantum Dot Solids by Trimethylaluminum Vapor Dosing”, *Applied Surface Science*, 513, 145812 (2020). The dissertation author was the primary investigator and author of this paper.

Chapter 3, in part or in full, is a reprint of the material as it appears in Applied Surface Science. S. T. Ueda, A. McLeod, D. Alvarez, D. Moser, R. Kanjolia, M. Moinpour, J. Woodruff, and A. C. Kummel, “Tris(dimethylamido)aluminum(III) and N_2H_4: Ideal precursors for the deposition of large grain, oriented c-axis AlN on Si via atomic layer annealing”, *Applied Surface Science*, 554, 149656 (2021). The dissertation author was the primary investigator and author of this paper.

Chapter 4, is in part or full, reprinted with permission from S. T. Ueda, A. McLeod, Y. Jo, J. Spiegelman, J. Spiegelman, D. Alvarez, D. Moser, R. Kanjolia, M. Moinpour, J. Woodruff, K. Cho, and A. C. Kummel, “Experimental and Theoretical Determination of the Role of Ions in Atomic Layer Annealing”, *manuscript submitted Journal of Materials Chemistry C*. The dissertation/thesis author was the primary investigator and author of this paper.

VITA

EDUCATION

2017 Bachelor of Science in Chemical Engineering, University of California San Diego

2018 Master of Science in Materials Science and Engineering, University of California San Diego

2021 Doctor of Philosophy in Materials Science and Engineering, University of California San Diego

PUBLICATIONS

S. T. Ueda, A. McLeod, Y. Jo, J. Spiegelman, J. Spiegelman, D. Alvarez, D. Moser, R. Kanjolia, M. Moinpour, J. Woodruff, K. Cho, and A. C. Kummel, "Experimental and Theoretical Determination of the Role of Ions in Atomic Layer Annealing," *Submitted to Journal of Materials Chemistry C.*

S. T. Ueda, A. McLeod, D. Alvarez, D. Moser, R. Kanjolia, M. Moinpour, J. Woodruff, and A. C. Kummel, "Tris(dimethylamido)aluminum(III) and N_2H_4: Ideal precursors for the deposition of large grain, oriented c-axis AlN on Si via atomic layer annealing," *Applied Surface Science*, 554, 149656 (2021).

S. T. Ueda, I. Kwak, A. Abelson, S. Wolf, C. Qian, M. Law, and A. C. Kummel, "Electronic Passivation of PbSe Quantum Dot Solids by Trimethylaluminum Vapor Dosing," *Applied Surface Science*, 513, 145812 (2020).

Z. Zhang, M. Passlack, G. Pitner, C.-H. Kuo, S. T. Ueda, H. Kashyap, V. Wang, J. Spiegelman, K.-T. Lam, A. C. Kummel, and P. R. Bandaru, "Sub-nanometer interfacial oxides on HOPG and CNTs enabled by lateral oxide growth," Submitted to *ACS Applied Electronic Materials*

Z.-W. Fang, H.-F. Luan, W. Tsai, K. Sardashti, M. Clemons, S. T. Ueda, M. Kavrik, I. Kwak, A. C. Kummel, and H.-P. Chang, "Nanolaminate structure, semiconductor device and method of forming nanolaminate structure," US Patent 10,840,350 (2020).

S. Wolf, M. Breeden, S. T. Ueda, J. Woodruff, M. Moinpour, R. Kanjolia, and A. C. Kummel, " The role of oxide formation on insulating versus metallic substrates during Co and Ru selective ALD," *Applied Surface Science*, 510, 144804 (2020).

M. Breeden, S. Wolf, S. T. Ueda, K. Tang, P. McIntyre, and A. C. Kummel, "Al2O3/Si0.7Ge0.3(001) & HfO2/Si0.7Ge0.3(001) Interface Trap State Reduction via In-Situ N2/H2 RF Downstream Plasma Passivation," *Applied Surface Science* 478, 101016 (2019).

M. S. Kavrik, E. Thomson, E. Chagarov, K. Tang, S. T. Ueda, V. Hou, T. Aoki, M. Kim, B. Fruhberger, Y. Taur, P. C. McIntyre, and A. C. Kummel, "Ultralow Defect Density at Sub-0.5 nm HfO_2/SiGe Interfaces via Selective Oxygen Scavenging," *ACS Applied Materials & Interfaces* 10 (36), 30794-30802 (2018).

I. Kwak, K. Sardashti, M. S. Clemons, S. T. Ueda, B. Fruhberger, S. Oktyabrsky, and A. C. Kummel, "HfO_2/Al_2O_3 Nanolaminate on $Si_{0.7}Ge_{0.3}$ (100) Surface by Thermal Atomic Layer Deposition," ECS Transactions 86 (7), 281 (2018).

K. Sardashti, E. Chagarov, P. D. Antunez, T. S. Gershon, S. T. Ueda, T. Gokmen, D. Bishop, R. Haight, and A. C. Kummel, "Nanoscale characterization of back surfaces and interfaces in thin-film kesterite solar cells," *ACS Applied Materials & Interfaces* 9 (20), 17024-17033 (2017).

FIELD OF STUDY

Major Field: Materials Science and Engineering

Studies in Surface Science and Physical Chemistry
Professor Andrew C. Kummel

ABSTRACT OF THE DISSERTATION

Materials Passivation and Synthesis Using Atomic Layer Deposition-Based Techniques

by

Scott Toshio Ueda

Doctor of Philosophy in Materials Science and Engineering

University of California San Diego, 2021

Professor Andrew C. Kummel, Chair

As traditional metal oxide semiconductor field effect transistors (MOSFETs) continue to be scaled to the atomic limit, the need for new materials and new passivation schemes to enable higher performance computing has continued to grow. Atomic layer deposition (ALD) has emerged as a potential solution for both thin film growth as well as materials passivation and because it occurs using surface reactions, the technique can be used in high aspect ratio, 3-dimensional structures commonly found in microelectronic circuits. This dissertation focuses on using variants of the ALD process for both materials passivation as well as materials synthesis.

In chapter two, ALD half cycles were used to passivate PbSe nanoparticle solid films. PbSe other lead chalcogenide (PbX, where X = S, Se, or Te) nanoparticles are of

increasing interest both in light emitting as well as light harvesting applications due to their tunable optoelectronic properties. Though the materials system holds great promise, progress so far has been limited by the poor carrier transport in these nanoparticle films. Though this poor carrier transport can be due to mesoscale defects in the nanoparticle film, the inherent instability of these materials in ambient conditions also presents a challenge to their continued adoption. Using scanning tunneling microscopy/spectroscopy (STM/STS), it is shown that dosing with half cycles of trimethyl aluminum was able to repair trace oxidation, as evidenced by the elimination of midgap states in STS as well as enhanced transistor performance.

In chapters three and four, a variant of ALD known as atomic layer annealing (ALA) was used to deposit crystalline, oriented AlN at low temperature and the mechanism of the ALA process is elucidated using both experimental as well as computational techniques. Crystalline AlN in particular is of interest due to the material properties of high thermal conductivity and high electrical resistivity. These materials can be used to eject heat from high density microelectronic circuits commonly found in logic applications or in high power circuits commonly found in radio frequency circuits. As power dissipation density in these circuits continues to increase, the ejection of heat becomes an increasingly important issue. Using ALA it is shown that high quality, crystalline films can be grown using the technique and by using both experimental techniques as well as molecular dynamics simulations, it is shown that ALA is a momentum transfer process. It is our hope that this better fundamental understanding of the process mechanism will lead to increased adoption of the process for other applications where the deposition of high quality crystalline materials is required.

Chapter 1

Introduction

1.1 Scaling of Metal Oxide Semiconductor Field Effect Transistors

Traditional metal oxide semiconductor field effect transistors (MOSFETs) fabricated out of silicon have formed the backbone of modern computing and though there has recently been a movement away from the exclusive use of silicon, namely with the addition of high mobility channel materials such as SiGe alloys [1], the continued scaling of these devices towards the atomic scale poses a finite limitation on the future of these devices [2]. The continued push for higher performance and lower power consumption necessitates the use of new materials and with that new passivation techniques for these new materials in the complex, 3-dimensional geometries commonly found in modern microelectronic architectures. Due to its ability to deposit high-quality, conformal films with precise thickness control at relatively low temperatures, atomic layer deposition (ALD) is an increasingly common technique for thin film deposition in semiconductor processing.

This goal of this dissertation is to describe non-traditional applications of ALD, that is, using variations of the traditional ALD dosing scheme to passivate a new class of materials consisting of nanoparticle solids and for the deposition of crystalline materials at low temperatures. To that end, this thesis is largely split into two parts: using half cycles of atomic layer deposition for the passivation of PbSe solids and on the use of a 3-step variant of atomic layer deposition known as atomic layer annealing for the deposition of crystalline aluminum nitride at low temperature.

1.2 Fundamentals of Atomic Layer Deposition

A typical ALD process consists of two, self-limiting half reactions where each precursor is dosed separately and sequentially (A-purge-B-purge pulse sequence). In the ideal case, each precursor chemisorbs to form a monolayer coverage and sequential cycles result in layer-by-layer growth with atomic-scale smoothness and conformal coverage. To prevent reactions in the gas phase, a pump or inert gas purge step typically follows each precursor dose; therefore, a prototypical ALD cycle consists of the following: (1) precursor A is introduced and chemisorbs with the sample surface, (2) an inert gas purge or pump step is run to remove excess unreacted precursor or reaction byproducts from the reaction chamber, (3) precursor B is introduced which also chemisorbs with the sample surface terminated in precursor A, and (4) an inert gas purge or pump step is run to remove excess unreacted precursor or reaction byproducts from the reaction chamber. These four steps comprise a typical ALD cycle and can be repeated any number of times to achieve the desired thickness. Fig. 1.1 contains a schematic of a generic ALD process using inert gas purge.

ALD processes generally have a finite temperature range over which self-limiting deposition occurs which is known as the 'ALD window' [3]. Outside of the ALD window, effects such as low reactivity or precursor desorption can lead to low growth rates with non-uniform coverage while other effects such as precursor decomposition or condensation can lead to high growth rates, resulting in non-conformal or rough films [4]. As the process window for most ALD processes is below ~ 400 °C, it is an attractive technique for back end of line processing, where thermal budgets are constrained to a maximum of ~ 450 °C.

1.3 Multi-chamber Vacuum System

The vacuum chamber used for the experiments in this thesis was an Omicron variable temperature (VT) ultra-high vacuum (UHV) chamber equipped with a scanning tunneling microscopy/spectroscopy (STM/STS) system. The UHV system consisted of two chambers pumped by ion pumps and titanium sublimation pumps which enabled base pressures of ~$5x10^{-10}$ Torr. The UHV chamber was additionally equipped with a non-monochromated X-ray photoelectron spectroscopy (XPS) system. Attached to the UHV chamber were a home-built plasma-enhanced ALD (PEALD) chamber and DC/RF sputter deposition system (Fig. 1.2). Samples were inserted into the turbomolecular-pumped load-lock and were transferred into one of the two deposition chambers before being analyzed in the UHV chamber. The PEALD chamber included a cryotrap was pumped via a turbomolecular drag pump with a base pressure of ~$8x10^{-7}$ Torr while the sputter deposition chamber was pumped by a turbomolecular pump with similar base pressure. The ALD chamber contained a stage heated with an external cartridge heater enabling maximum substrate temperatures ~600 °C while also allowing for the use of DC or RF substrate biasing. The sputter deposition chamber used a multipurpose manipulator capable of substrate heating or cooling. ALD pulsing was controlled using pneumatically actuated diaphragm valves while the gas flows for both chambers were managed using mass flow controllers.

Using this multi-chamber vacuum system allowed for the deposition and characterization of a variety of thin films *in vacuo* with minimal surface oxidation or contamination. Although films can be removed from vacuum and undergo processes such as high vacuum annealing or Ar sputtering, these processes are destructive and can often

convolute experimental results which makes it less favored when compared to a tool that can perform everything *in vacuo*. In the PEALD chamber, both thermal ALD or plasma processes could be run using Ne, Ar, Kr, N_2, or NH_3 gas and any variety of two room temperature sources and two hot sources. Examples of precursors used on the system include N_2H4, TMA, TEGa, and NH_3 (liquid sources) and TDMAA, TDMAGa, $AlCl_3$, and AlH_2 (hot sources). The plasma system consisted of a PIE remote plasma source with quartz tube that could be used for plasma cleaning, PEALD, or ALA. Ion energy could be tuned using a DC or RF biasing system incorporated into the stage design.

1.4 Scanning Tunneling Microscopy

STM was originally developed in 1981 by Binnig and Rohrer to study the surfaces of metals and semiconductors with atomic resolution [5-7]. The technique was used in chapter two of this thesis to study surface morphology, long range order of nanoparticle superlattices, and as an indirect measure of surface ligand coverage. The measurement setup is generally quite simple and as shown in Fig. 1.3, consists of an atomically sharp tip usually fabricated out of electrochemically etched tungsten. A small bias of ~2 V is applied to the tip and once the tip is approached to within a few angstroms of the substrate, a small tunneling current can be measured. This tunneling current increases exponentially as the tip-sample separation decreases and so by maintaining a constant tunneling current (using feedback electronics), surface topography and density of state (DOS) can be probed as the tip is scanned across the sample.

When a negative bias is applied to the tip relative to the sample, electrons tunnel from the filled orbitals of the tip into the empty unoccupied orbitals of surface atoms

(empty state imaging). Conversely, when a positive bias is applied to the tip relative to the sample, electrons from filled substrate atom orbitals tunnel into unoccupied orbitals of the tip (filled state imaging). Using this technique, atomic resolution images can be obtained; however, for many studies, the local DOS (LDOS) is the object of interest and so a complimentary type of measurement known as scanning tunneling spectroscopy (STS) is used.

1.5 Scanning Tunneling Spectroscopy

STS is a complimentary technique to STM used to probe LDOS where instead of scanning across the sample surface to generate an image, the tip is paused over a single point and the voltage of the tip is swept while tunneling current is measured. To accomplish this measurement, the tip is positioned over the area of interest, the height is fixed, and the tip bias is modulated from ~ -2 V to ~ +2 V. While this measurement is taking place, a lock-in amplifier is used to superimpose an AC signal over the DC bias and the resulting in-phase AC component of the modulation voltage is used to extract the differential conductance (dI/dV). After normalizing this differential conductance to $\overline{I/V}$, the resultant normalized differential conductance is proportional to the LDOS at the point where the spectra were taken [8]. The (dI/dV)/$\overline{I/V}$ spectra are then fit using a linear fit function described in detail by Feenstra *et al.* [9-10] to determine the onset bias relative to the Fermi level.

Using the STS spectra, band gap energy, Fermi level (defined as 0 V bias) position, and conductance band and valance band edges can be determined as can the presence of states inside of the band gap. Using this technique both before and after sample treatment

provides great insight as to changes in the electronic structure of the material and can help elucidate the effectiveness of the passivation scheme being studied. Along with the removal of mid gap states, a common proxy for the removal of defects is Fermi level depinning whereby a Fermi level that was once pinned (not able to be modulated due to the presence of surface states in the band gap) becomes modulable once those defects are passivated or removed [11].

1.6 X-Ray Photoelectron Spectroscopy

XPS is a method of determining the surface chemical composition of a sample and as used extensively throughout all three chapters of this thesis. XPS relies on the photoelectric effect whereby an incident photon with known kinetic energy generates electron emission with a characteristic kinetic energy that is a function of the incident photon kinetic energy, the binding energy of the electron being release, and the work function of the spectrometer performing the measurement [12]. Briefly, the experimental setup uses a tungsten filament that is heated to generate electron emission. A Mg anode is biased at a potential of ~ 15 kV and as the electrons from the filament strike the anode, Mg Kα x-rays ($h\nu$ = 1253.6 eV) are emitted. These x-rays pass through an Al window to out Bremsstrahlung radiation [13] and are then directed towards the sample. Under photon flux, core and valence electrons are emitted from the sample which are in turn collected by the electron analyzer. The electron analyzer used in this thesis was a double pass cylindrical mirror analyzer that used two concentric cylindrical anodes held at different potential to filter electrons by kinetic energy. After passing through electrons of a given energy, they reach the detector where the signal is multiplied and fed to a preamplifier to convert the

data into a spectrum of counts as a function of energy. Though the kinetic energy is the physically measured quantity, this value can easily be converted to the electron binding energy using the following equation:

$$KE_{electron} = E_{h\upsilon} - BE_{electron} - \Phi_{spec}. \qquad (1.5.1)$$

The chemical shift of the binding energy of an electron gives great insight into the local bonding environment (reduction or oxidation of a particular species being studied) and in addition, XPS may be used to perform saturation studies or calculate overlayer thickness by measuring substrate attenuation.

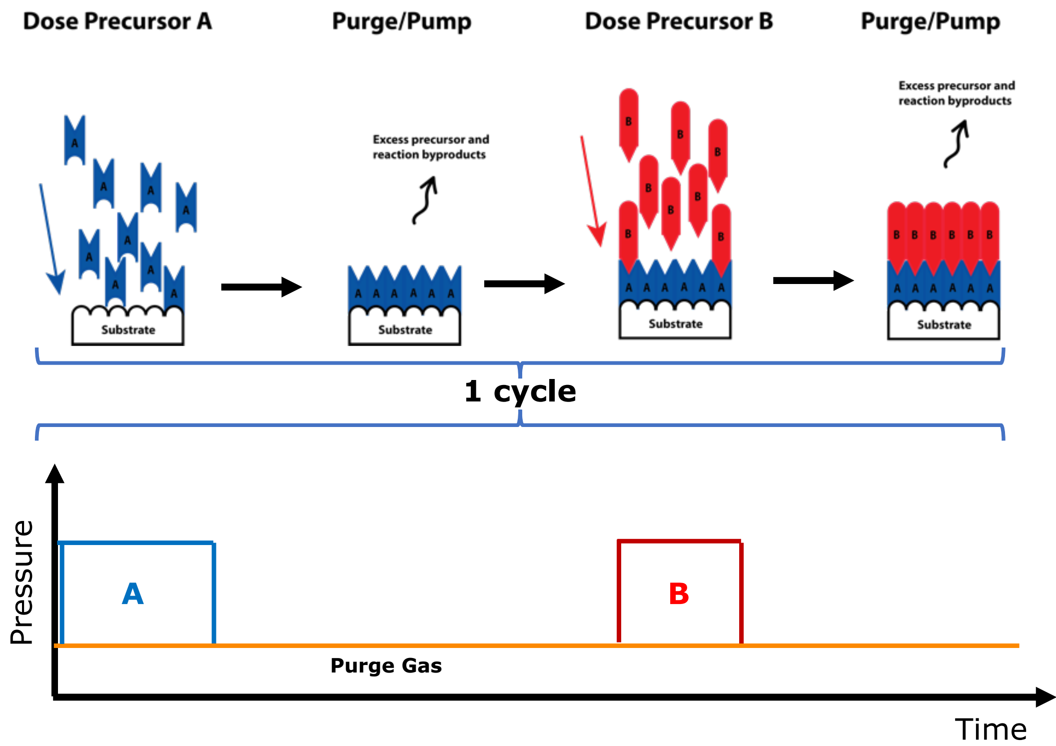

Figure 1.1 Schematic diagram of a prototypical ALD process. Precursor A is dosed resulting in a self-saturating monolayer. After a purge/pump step to remove excess precursor A and reaction byproducts, precursor B is dosed which results in the addition of a monolayer of precursor B chemisorbed to the surface. This results in a high-quality, conformal film and the cycle can be repeated any number of times to achieve the desired film thickness.

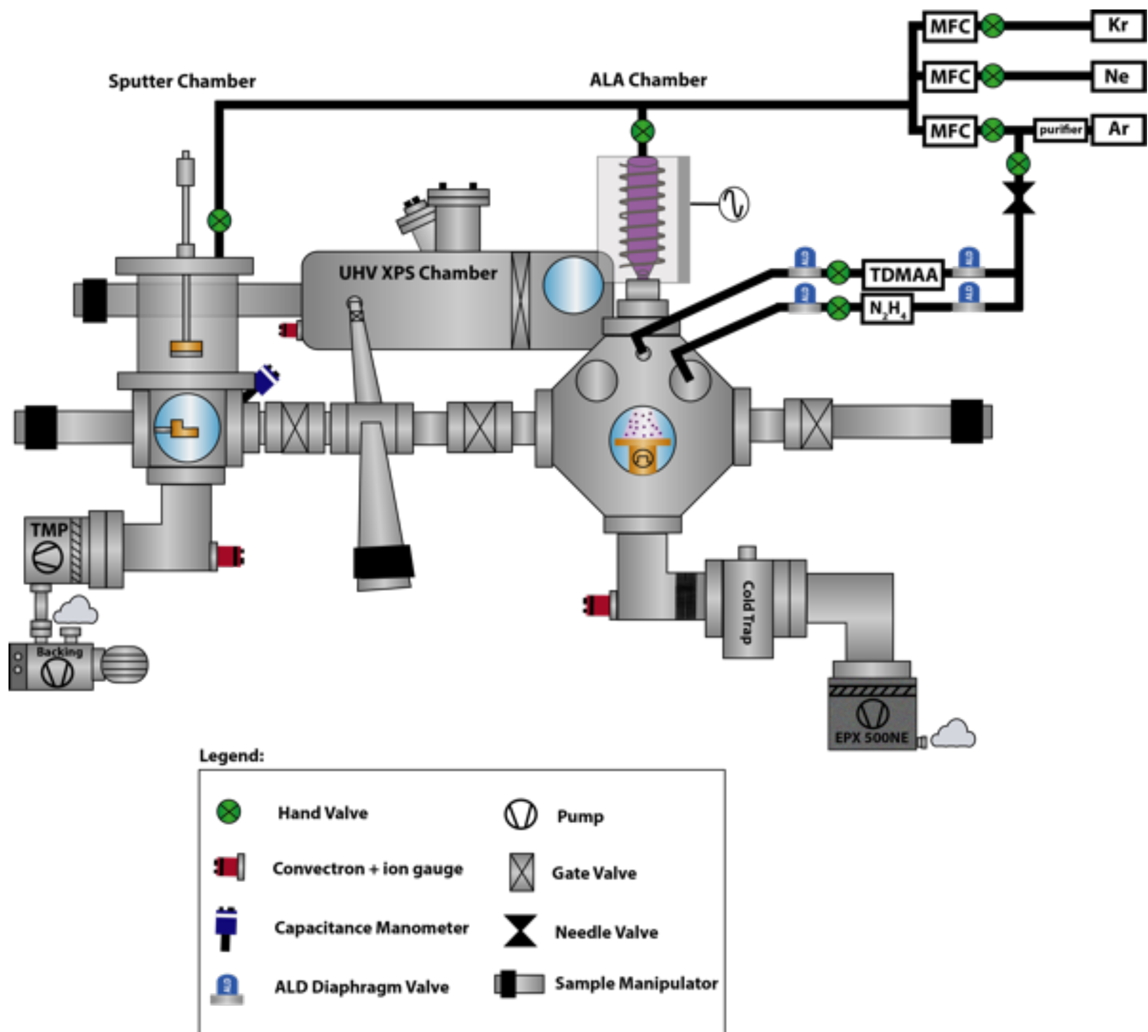

Figure 1.2 Schematic diagram of the multi-chamber vacuum system. The UHV chamber contains both XPS as well as STM/STS. A sputter deposition system with one gun (DC or RF) is attached to the UHV system as is a custom PEALD chamber with cold trap and sample biasing capability.

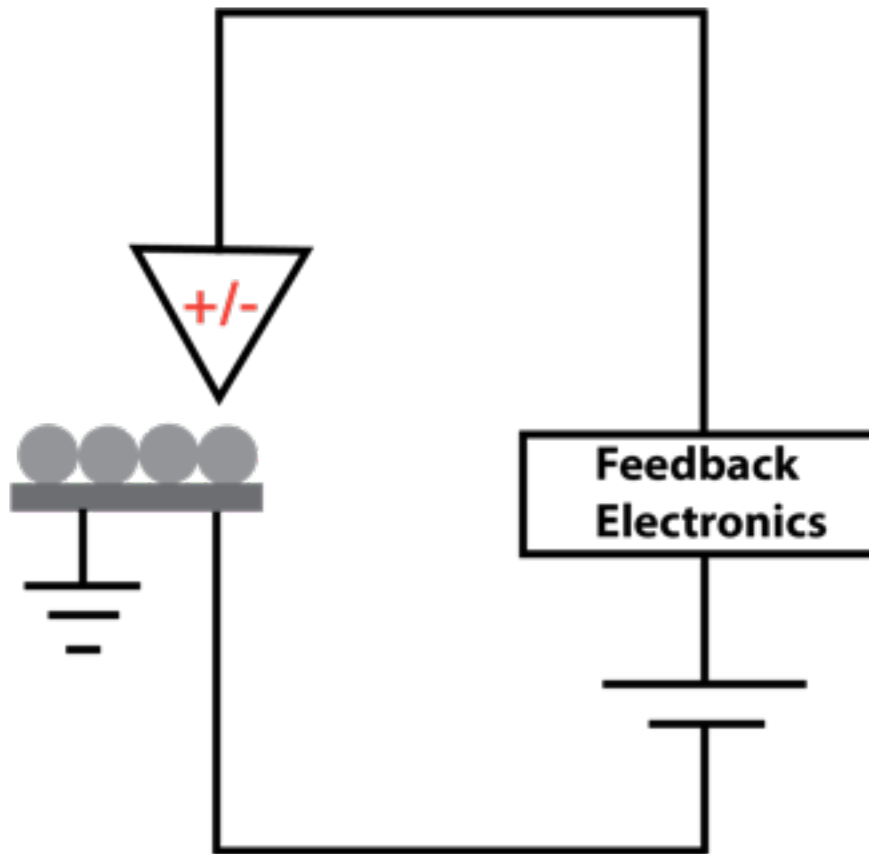

Figure 1.3 Schematic diagram a typical STM imaging circuit. In filled state imaging the tip will be biased positively with respect to the substrate, causing electrons to tunnel from filled orbitals of the sample surface into empty state orbitals of the tip. In empty state imaging the tip is biased negatively with respect to the sample, and electrons tunnel from filled states of the tip into empty unfilled states of the sample surface. The feedback electronics adjust tip-sample spacing to maintain constant tunneling current while the tip scans across the sample surface.

1.6 References

[1] Kuhn, K. J.; Murthy, A.; Kotlyar, R.; Kuhn, M. (Invited) Past, Present and Future: SiGe and CMOS Transistor Scaling. *ECS Trans.* **2019**. https://doi.org/10.1149/1.3487530.

[2] Shalf, J. M.; Leland, R. Computing beyond Moore's Law. *Computer (Long. Beach. Calif).* **2015**. https://doi.org/10.1109/MC.2015.374.

[3] Johnson, R. W.; Hultqvist, A.; Bent, S. F. A Brief Review of Atomic Layer Deposition: From Fundamentals to Applications. *Materials Today*. 2014. https://doi.org/10.1016/j.mattod.2014.04.026.

[4] George, S. M. Atomic Layer Deposition: An Overview. *Chem. Rev.* **2010**. https://doi.org/10.1021/cr900056b.

[5] Binnig, G.; Rohrer, H. Scanning Tunneling Microscopy from Birth to Adolescence. *Rev. Mod. Phys.* **1987**. https://doi.org/10.1103/RevModPhys.59.615.

[6] Binnig, G.; Rohrer, H. SCANNING TUNNELING MICROSCOPE. *Sci. Am.* **1985**. https://doi.org/10.1038/scientificamerican0885-50.

[7] G. Binnig; Rohrer, H. SCANNING TUNNELING MICROSCOPY G. BINNIG and H. ROHRER. *Surf. Sci.* **1983**.

[8] Stroscio, J. A.; Feenstra, R. M.; Fein, A. P. Electronic Structure of the Si(111)2 × 1 Surface by Scanning-Tunneling Microscopy. *Phys. Rev. Lett.* **1986**. https://doi.org/10.1103/PhysRevLett.57.2579.

[9] Feenstra, R. M. Tunneling Spectroscopy of the (110) Surface of Direct-Gap III-V Semiconductors. *Phys. Rev. B* **1994**. https://doi.org/10.1103/PhysRevB.50.4561.

[10] Feenstra, R. M.; Lee, J. Y.; Kang, M. H.; Meyer, G.; Rieder, K. H. Band Gap of the Ge (111) c (2×8) Surface by Scanning Tunneling Spectroscopy. *Phys. Rev. B - Condens. Matter Mater. Phys.* **2006**. https://doi.org/10.1103/PhysRevB.73.035310.

[11] Feenstra, R. M.; Mårtensson, P. Fermi-Level Pinning at the Sb/GaAs(110) Surface Studied by Scanning Tunneling Spectroscopy. *Phys. Rev. Lett.* **1988**. https://doi.org/10.1103/PhysRevLett.61.447.

[12] Hollander, J. M.; Jolly, W. L. X-Ray Photoelectron Spectroscopy. *Acc. Chem. Res.* **1970**. https://doi.org/10.1021/ar50030a003.

[13] Stevie, F. A.; Donley, C. L. Introduction to X-Ray Photoelectron Spectroscopy. *J. Vac. Sci. Technol. A* **2020**. https://doi.org/10.1116/6.0000412.

Chapter 2

Electronic passivation of PbSe quantum dot solids by trimethylaluminum vapor dosing

2.1 Abstract

The inherent instability of PbSe quantum dot (QD) thin films in ambient atmospheric conditions presents a significant challenge to their use in devices. Using low-temperature scanning tunneling microscopy and scanning tunneling spectroscopy, the electronic passivation of epitaxially-fused PbSe QD superlattices (epi-SLs) by trimethylaluminum (TMA) vapor dosing was studied. TMA dosing immobilizes loosely bound mobile adsorbates and passivates states on the surface of the QDs. X-ray photoelectron spectra of QD films prepared by dip coating show an aluminum surface concentration of <1% of a monolayer, consistent with the TMA binding only to defect sites. Field-effect transistor (FET) transport measurements of similar films confirm the impact of this trace surface state passivation. QD FETs dosed with TMA show a shift from *p*-channel to *n*-channel behavior as well as a 20-fold increase in mobility and 300-fold increase in on/off ratio compared to devices before TMA dosing. Defect passivation by TMA vapor dosing may facilitate the integration of PbSe QD solids into future optoelectronic devices.

2.2 Introduction

Lead chalcogenide (PbX, where X = S, Se, or Te) quantum dots (QDs) are of interest for next-generation electronic and optoelectronic devices due to their tunable optical and electrical properties and enhanced ability to generate multiple excitons per

photon compared to their bulk semiconductor counterparts [1], [2], [3], [4]. Enhanced multiple exciton generation (MEG) opens the door to highly-efficient photovoltaics, and several groups report efficient MEG for colloidal PbX systems [5], [6], [7], [8], [9]. Superlattices (SLs) composed of "confined-but-connected" or "epitaxially fused" QDs (epi-SLs) are expected to generate bulk-like electronic mini-bands and exhibit high carrier mobility and diffusion length compared to conventional weakly-coupled QD solids [2], [10], [11]. Physical and electronic coupling between the QDs is achieved by exchange of oleate ligands with smaller ligands such as SCN^{-}, S^{2-}, or ethylene glycoxide that cause necking (limited crystallographic fusion) of the QDs [12], [13], [14], [15]. Despite strong electronic coupling, charge transport in epi-SLs can be severely limited by surface states [16] arising from undercoordinated surface atoms, non-stoichiometry, ligands, weakly-bound adsorbates, or oxidation [17], [18], [19].

In this work, the local densities of states of monolayer (2D) and bilayer epi-SLs of PbSe QDs were measured by low-temperature scanning tunneling microscopy/spectroscopy (STM/STS) in ultra-high vacuum (UHV), and it was demonstrated that in vacuo dosing with trimethylaluminum (TMA) vapor improves STM imaging and passivates surface states to yield an electronically unpinned QD surface. X-ray photoelectron spectra of similar TMA-dosed samples showed a very small aluminum coverage (<1% of a monolayer), indicating that TMA binds to only a small fraction of surface sites, which was hypothesized to be the most active surface defect states. TMA dosing also improved the performance of PbSe QD field-effect transistors (FETs). TMA-dosed FETs showed a shift from p-channel to n-channel behavior as well as a 20-fold

increase in mobility and 300-fold increase in on/off ratio compared to devices without TMA dosing.

2.3 Experimental

2.3.1. Materials

All chemicals were used as received unless otherwise noted. Lead oxide (PbO, 99.999%) and selenium shot (99.999%) were purchased from Alfa Aesar. Trimethylaluminum (TMA, 98%) was purchased from both Strem Chemicals and Sigma Aldrich. Oleic acid (OA, technical grade, 90%), 1-octadecene (ODE, 90%), diphenylphospine (DPP, 98%), anhydrous hexanes (99%), anhydrous ethanol (99.5%), anhydrous toluene (99.8%), anhydrous octane (≥99%), anhydrous acetonitrile (99.99%), anhydrous isopropanol (IPA, 99.5%), anhydrous tetrachloroethylene (TCE, 99%), acetone (99.9%), ammonium thiocyanate (NH_4SCN, 99.99%), and 3-mercaptopropyltrimethoxysilane (3-MPTMS, 95%) were purchased from Sigma Aldrich. Trioctylphosphine (TOP, technical grade, >90%) was purchased from Fluka and mixed with selenium shot over a period of 24 h to create a 1 M TOP-Se stock solution. Prior to use, the NH_4SCN was purified via recrystallization in anhydrous isopropanol.

2.3.2. Quantum dot synthesis

Oleate-capped PbSe quantum dots with a diameter of 6.5 nm were synthesized using standard air-free techniques. In a typical synthesis, PbO (1.5 g), oleic acid (5.0 g), and ODE (10.0 g) were mixed and degassed thoroughly in a three-neck round-bottom flask at room temperature. The mixture was heated to 110 °C in vacuum to form $Pb(OA)_2$ and

to dry the solution. After 1.5 h, the $Pb(OA)_2$ solution was heated to 180 °C in flowing argon, then 9.5 mL of a 1 M solution of TOP-Se containing 200 µL of DPP was rapidly injected into the hot solution. The QDs were grown at ~150 °C for 105 s, at which point the reaction was quenched with a liquid nitrogen bath and the injection of 10 mL of anhydrous hexanes. The QDs were purified in a N_2-filled glovebox (<0.5 ppm O_2) by three rounds of precipitation/redispersion using ethanol/hexane, then dispersed in toluene (1.75 g L^{-1}) for film fabrication.

2.3.3. Basic characterization

Optical extinction measurements of QDs dispersed in TCE were performed air-free with a PerkinElmer Lambda 950 spectrophotometer. Neat TCE served as the background for the solution measurements. The QD diameter and polydispersity were determined using the empirical relationship of Moreels et al. [20]. Scanning electron microscopy (SEM) was performed on an FEI Magellan 400L SEM operating at 10 kV and 25 pA.

Small angle X-ray scattering (SAXS) measurements were performed on Beamline 7.3.3 of the Advanced Light Source (ALS) at Lawrence Berkeley National Laboratory using 10 KeV monochromatic X-rays (λ = 1.24 Å) with an energy bandwidth of 1%. A Dectris Pilatus 2 M detector with a pixel size of 0.172 × 0.172 mm and 1475 × 1679 pixels was used to record the 2D scattering patterns. A silver behenate standard was used to determine the sample-to-detector distance and beam center. For solution SAXS measurements, a 30 gL^{-1} octane suspension of QDs was drawn into a 2 mm × 0.2 mm glass capillary with a 0.150 mm wall thickness (Electron Microscopy Sciences). The solution was exposed to air briefly before and during measurement. The sample-to-detector distance

was 2994.78 mm as calibrated by the silver behenate standard. Signal was collected for 120 s, and an octane-filled blank capillary was used for background subtraction. The Nika software package [21] in Igor Pro was used to azimuthally integrate (25–75°) the SAXS pattern and correct for the background using the octane-filled blank. Particle distribution fitting was performed using a spherical form factor with a Gaussian spread of QD diameters in the NIST SANS Analysis package [22] in Igor Pro. No instrumental broadening was included in the fitting procedure, which indicates that the reported polydispersity is likely an overestimation.

2.3.4. Scanning tunneling microscopy

Sub-monolayer QD films were prepared by dip coating in a N_2-filled glovebox (<5 ppm O_2) adjacent to the STM instrument. First, oleate-capped PbSe QDs dispersed in toluene were dip coated onto a mechanically-exfoliated highly oriented pyrolytic graphite (HOPG) substrate. Once the toluene fully evaporated, the substrate was immersed in a 4 mM solution of NH4SCN in acetone to trigger ligand exchange and epi-SL formation. The substrate was rinsed for 10 s in anhydrous acetonitrile, hexane, and again in acetonitrile to remove free ligands, dried, and transferred into a commercial Omicron VT UHV STM (base pressure = 1×10^{-11} Torr) using a glove bag purged with N_2 to avoid air exposure. These samples were first measured before TMA exposure, then transferred in vacuo to an attached ALD chamber (base pressure ~10^{-6} Torr), dosed with TMA using multiple 350 mTorr pulses (total TMA dose of $2–8 \times 10^6$ Langmuir), and transferred back to the STM chamber without air exposure.

STM topography images were acquired with a tungsten tip prepared by electrochemical etching of a tungsten wire. Images were acquired at 100 K in constant current mode (I = 0.03 nA) with a tip bias of +2 V. Scanning tunneling spectroscopy (STS) was performed at 100 K to investigate the electronic structure of the QDs using variable z-mode over a bias range of −1 to 1 V. To determine the onset bias relative to the Fermi level (i.e., the valence and conduction band edge energies) from the (dI/dV)/(I/V) curves, STS curve fitting was employed as described in detail by Feenstra et al. [23], [24].

2.3.5. X-ray photoelectron spectroscopy

Multilayer QD films for XPS characterization were deposited by manual layer-by-layer dip coating [25] at UC San Diego using the same NH_4SCN solution used to fabricate the STM/STS samples. These discontinuous films were amorphous (i.e., minimal QD positional order and epi-SL grains). The samples were transferred with minimal air exposure via glove bag to a monochromatic XPS system (Al Kα, hν = 1486.7 eV). XP spectra were acquired at a collection angle of 60° relative to the surface normal at a pass energy of 50 eV and step width of 0.1 eV. Analysis of the XPS data was performed in CasaXPS v2.3 using Shirley background subtraction and Schofield photoionization cross sectional relative sensitivity factors.

2.3.6. Field-effect transistor measurements

Multilayer QD film field-effect transistor (FETs) employed a bottom contact (5 nm Ti, 35 nm Au), global back gate geometry (p^{++} Si, 200 nm SiO_2, C_{ox} = 17.5 nF/cm^2) with a channel length of 25 μm and width of 1000 μm. FET substrates were cleaned by successive

sonication in acetone, Millipore water, and IPA, blown dry with air, then treated with 15 min of O_2 plasma cleaning. The substrates were transferred into the glovebox and soaked in a 100 mM solution of 3-MPTMS in toluene for 1 h to improve QD adhesion, rinsed vigorously in neat toluene and dried in flowing nitrogen. Automated layer-by-layer dip coating of QD films was performed at UC Irvine using a Nima DC-4 dip coater in the glovebox. Substrates were dipped into a 3.9 gL^{-1} dispersion of QDs in hexane, followed by a 12 s soak in a 15 mM solution of NH_4SCN in acetonitrile and finally a 3 s soak in neat acetonitrile. This process was repeated 10 times to generate ~40 nm thick QD films. The FETs were dosed with TMA in a low-vacuum ALD system (base pressure ~10^{-2} Torr) integrated into the glovebox. TMA was dosed for 100 ms (10^5–10^6 Langmuir) using a computer-controlled diaphragm valve. FETs were measured in the glovebox (<0.1 ppm O_2) using a Keithley 2636B source-measure unit controlled by home-built LabView software. All measurements were performed at room temperature using a sweep rate of ~40 V/s to minimize artifacts from the bias-stress effect.

2.4 Results and Discussion

2.4.1 Basic quantum dot film characterization.

Figure 2.1a shows an optical extinction spectrum of a suspension of the oleate-capped PbSe QDs used in this study (diameter of 6.6 ± 0.4 nm, band gap of 0.674 eV). The QD diameter was determined using both small angle X-ray scattering and the empirical sizing curve of Moreels et al.[20]. Sub-monolayer to bilayer thick films of these QDs were formed by controlled evaporation of a toluene suspension on freshly exfoliated highly-oriented pyrrolitic graphite (HOPG) substrates (see Methods). Once dry, the samples were

immersed in a solution of ammonium thiocyanate in acetone to exchange the native oleate ligands and generate the epitaxially-fused SLs shown by SEM imaging in Figure 2.1b [26]. These samples feature small (10-100 nm) 2D epi-SL grains scattered across the substrate. The SL grains consist of 1-2 monolayers of QDs that are epitaxially connected across their {100} facets to form quasi-square lattices, similar to the structure of previously-reported 2D epi-SLs [27-28]. Figure 2.1c is a representative scanning tunneling microscopy (STM) topography image of a smaller area of one of these samples showing that the quasi-square SL is clearly resolved.

2.4.2 Scanning tunneling microscopy measurements of quantum dot film before and after TMA dosing

Figure 2.2 presents STM images of an epi-SL sample before and after *in vacuo* dosing with 2×10^6 L of TMA vapor at room temperature. Before TMA dosing, the STM images exhibited temporal instability, scan artifacts, and high noise (Fig. 2.2a). After dosing, STM image quality was significantly enhanced (Fig. 2.2b). The improvement was quantified by measurement of the RMS surface roughness averaged over several QDs, which decreased from 0.28 to 0.15 nm. An increase in noise when surface adsorbates attach to STM tips is a well-known phenomenon that likely arises from adsorbates on the tip changing conformation during the scan, leading to instabilities in the tunneling current [29]. Therefore, the improved image sharpness and decrease in RMS roughness is attributed to TMA-facilitated immobilization or removal of weakly-bound adsorbates such as physisorbed water and hydroxyl groups.

2.4.3 Scanning tunneling spectroscopy measurements of quantum dot film before and after TMA dosing

The local density of states (LDOS) of 40 QDs in the monolayer epi-SL grains was measured as a function of TMA dosing (Figure 2.3). STS traces were acquired at the center of the top {100} facet of each QD. Qualitative comparison of the normalized differential conductance $(dI/dV)/(I/V)$ versus voltage traces before and after TMA dosing shows that the TMA treatment significantly increases the electrical band gap of the QDs (Fig. 2.3a). The band gap value were calculated from fits of the STS data following Feenstra et al. [23-24]. Before TMA dosing, the measured band gap is 0.35 ± 0.07 eV, which is 0.32 eV smaller than the optical band gap of the QDs in solution (Fig. 2.1a) and 0.30 eV smaller than the optical band gap of the ligand-exchanged QD films. Figure 2.3b plots the electrical band gap versus the TMA dose. The band gap increases with increasing TMA dose until a dose of $\sim 5 \times 10^6$ L, where it saturates at 0.65 ± 0.06 eV, close to the value of the optical band gap (Fig. 2.3b). This behavior is consistent with the passivation of gap states by TMA ostensibly via the reduction of trace selenium oxides that are known to create defect states and dangling bonds on PbSe QDs [17-18, 30]. Defect-induced band gap narrowing has been found on many other surfaces, including PbS QDs, [31] where density functional theory was used to model the generation of weakly-conductive midgap states caused by Pb:S off-stoichiometry, and Ge(100), where STM/STS was used to investigate H_2O_2 passivation of Ge dangling bonds [32].

Figure 2.4a-d show pre- and post-TMA STS curves from mono- and bi-layer portions of the QD SL. The extracted difference between the intrinsic Fermi level and measured Fermi level of each sample (E_i-E_F) is compiled in Figure 2.4e. The total TMA

dose was approximately 5×10^6 L, which is the same dose required to restore the band gap (see Fig. 2.3). STS traces were recorded on tens of QDs in each layer before and after dosing. Before TMA dosing, the QDs displayed predominantly *p*-type behavior (E_i-E_F = 0.11 ± 0.08 eV with E_g = 0.35 eV) in monolayer portions of the films and E_i-E_F = 0.14 ± 0.07 eV in bilayers (Figure 2.4a-b). After TMA dosing, QDs in the monolayer became intrinsic (E_i-E_F = 0.05 ± 0.11 eV with E_g = 0.65 eV) while those in the bilayer remained *p*-type (E_i-E_F = 0.22 ± 0.06 eV). This Fermi level difference is consistent with band bending at the QD-HOPG interface. Prior to TMA treatment, the Fermi level may be pinned by surface defects (e.g., surface oxides), as was reported previously [33-34]. Following TMA treatment, the surface states are passivated, and the Fermi level becomes unpinned. Figure 2.4f-g show band diagrams for both situations. Due to the smaller work function of the HOPG substrate relative to the QDs, downward band bending will occur in the QD layer when the Fermi level is unpinned (Fig. 2.4f). This band bending causes QDs in the first monolayer (at the QD-HOPG interface) to appear more intrinsic while those in the second monolayer appear more *p*-type, in line with our measurements of TMA-dosed samples. However, if the Fermi level is pinned by surface states with energies near the valence band edge, then E_i-E_F should be independent of QD layer, as observed for samples before TMA dosing (Fig. 2.4g).

2.4.4 XPS Study of QD surface oxidation

X-ray photoelectron spectroscopy was performed to determine the coverage of TMA reaction products on the surface of multilayer QD films made by dip coating (see Methods). Multilayer amorphous films were used for XPS because the mono-/bi-layer

films used for STM/STS studies were too sparse to produce high signal-to-noise XP spectra. Figure 2.5 shows high-resolution XP spectra of the Pb 4f, Se 3d, O 1s, and Al 2p regions and quantification of the detected elements (Pb, Se, and C). It was expected that Al from TMA would bind to the surface of the QDs and be detectable by XPS. However, no aluminum or oxygen signal was observed before or after TMA dosing (Fig. 2.5d-e). Although there is no detectable oxygen and the chemical shift of Pb and Se suggest purely Pb-Se bonding without a large coverage of surface oxides, oxygen is a known acceptor in PbX QD films [35-36] and can likely dope the QDs at concentrations below the detection limit of XPS [17, 37-41]. The absence of oxygen signal, the chemical shift of the carbon peak (Fig. 2.5c), and SEM imaging of an identically prepared sample indicate that the large carbon signal originates from the HOPG substrate and not residual oleate ligands or adventitious hydrocarbons. The XPS data are consistent with TMA passivating surface states and/or removing ligands with a density below 10^{13} cm^{-2}, which is 10× more than required to pin the Fermi level but still below the detection limit of XPS [42].

2.4.5 Thermodynamic analysis of TMA reaction with trace oxides on PbSe

A simple thermodynamic analysis can be employed to show that TMA is likely to react with all surface oxides. The primary oxidation products of PbSe QDs are PbO, SeO_2, and $PbSeO_3$ [18,43,44], as shown in equations 1-3:

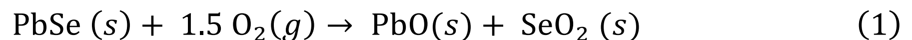

$$\mathrm{PbSe}\,(s) + 1.5\,\mathrm{O_2}(g) \rightarrow \mathrm{PbO}(s) + \mathrm{SeO_2}\,(s) \quad (1)$$

$$\mathrm{PbSe}\,(s) + 1.5\,\mathrm{O_2}(g) \rightarrow \mathrm{PbSeO_3}(s) \quad (2)$$

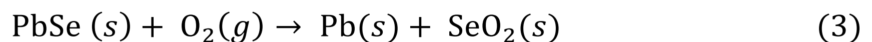

$$\mathrm{PbSe}\,(s) + \mathrm{O_2}(g) \rightarrow \mathrm{Pb}(s) + \mathrm{SeO_2}(s) \quad (3)$$

Proposed mechanisms for the surface reaction of TMA and reduction of trace surface oxides are the following:

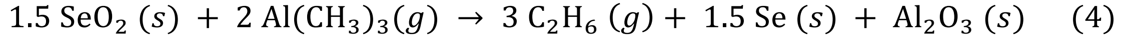

$$1.5\ SeO_2\ (s)\ +\ 2\ Al(CH_3)_3(g)\ \rightarrow\ 3\ C_2H_6\ (g) +\ 1.5\ Se\ (s)\ +\ Al_2O_3\ (s) \quad (4)$$

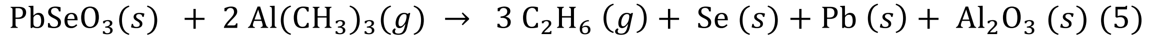

$$PbSeO_3(s)\ +\ 2\ Al(CH_3)_3(g)\ \rightarrow\ 3\ C_2H_6\ (g) +\ Se\ (s) + Pb\ (s) +\ Al_2O_3\ (s) \quad (5)$$

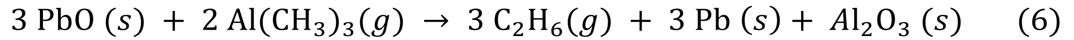

$$3\ PbO\ (s)\ +\ 2\ Al(CH_3)_3(g)\ \rightarrow\ 3\ C_2H_6(g)\ +\ 3\ Pb\ (s) +\ Al_2O_3\ (s) \quad (6)$$

In reactions (4-6), the primary driving force for the reduction of surface oxides is the formation of aluminum oxide. Using known heats of formation, the reaction enthalpies for reactions (4-6) are calculated to be -1392 kJ/mol, -1217 kJ/mol, and -1091 kJ/mol indicating it is thermodynamically favored for TMA to react with all three of the common oxidation products on the surface of the QDs, thereby passivating defect states that are known to arise from the presence of mixed Se-containing oxides [19,30]. The electronic passivation of semiconductor surfaces via the reduction or removal of surface oxides and adsorbed water by TMA is favored by the large formation enthalpy of Al_2O_3 and is consistent with the so-called “TMA clean-up effect” observed for many semiconductors including GaAs [45-46], InAs [47], and Ge [48].

2.4.6 Field Effect Transistor Measurements

Field-effect transistors (FETs) were fabricated to independently assess the impact of TMA dosing on the electronic properties of multilayer QD films. A cartoon of the FET geometry is provided in Figure 2.6a. Pre-TMA devices exhibited significant drain current transients (Fig. 2.6b) resulting from the bias-stress effect [49]. Figures 2.6c-d show output

and transfer characteristics of these devices, which were *p*-channel with I_{on}/I_{off} = 1.5 (at V_{SD} = -10 V and V_G = 0 vs. -40 V) and a linear hole mobility $\mu_{lin,h}$ = 0.07 cm^2/Vs. The FETs were dosed with TMA and immediately remeasured. These TMA-treated FETs (Fig. 2.6e-f) were dominant *n*-channel devices, I_{on}/I_{off} = 440, $\mu_{lin,e}$ = 1.4 cm^2/Vs, and improved drain current stability (see Fig. 2.6b). The 20-fold increase in mobility is likely due to the change in carrier polarity [50] and removal of in-gap defect states by TMA, in agreement with the STM/STS results demonstrating an unpinned Fermi level following TMA exposure. The 300-fold increase in on/off ratio results primarily from a decrease in I_{off} that we attribute to the passivation of shallow defect states associated with trace surface oxides.

Similarly large increases in mobility have been observed by passivating trap states in transition metal chalcogenide QD devices using methods such as indium diffusion doping of CdSe QDs [51] and ALD alumina infilling of PbSe QDs [16]. However, this study is unique because it shows that trace amounts of surface oxidation (below XPS detection limits) are present even on ligand-exchanged QDs fabricated using "air-free" techniques and that TMA can effectively repair these defects. Additional experiments on PbSe QDs treated with 1,2-ethanedithiol (EDT) instead of NH_4SCN demonstrate a compairtively minor improvement in FET performance. The FET data in Figure 2.6 are consistent with TMA eliminating surface oxidation products that result from exposure to trace oxygen and water during QD synthesis, purification, and storage [52]. These surface oxides generate high conductivity and *p*-channel behavior in PbSe QD films, which is in agreement with both the *p*-type behavior observed prior to dosing in the STS studies and the FET data [40]. By eliminating trace defect states with TMA dosing, both the carrier mobility and on/off ratio increase by 1-2 orders of magnitude.

2.5 Conclusions

TMA dosing provides a facile means to remove trace surface oxides on PbSe QD films and yields insight into the origin and impact of electronic defects in these mateirals. Dosing with TMA was found to improve STM image quality, passivate defects, widen the local band gap, unpin the Fermi level, and improve charge transport and transistor performance, consistent with the removal of surface oxides and/or adsorbates present at coverages below 1% of a monolayer. XP spectra lacked Al and O signal following defect removal by TMA, demonstrating the low surface density of these defect states. Transistors were used to show the impact of this trace defect removal on charge transport. FETs exposed to TMA show a shift from *p*-channel to *n*-channel behavior as well as large increases mobility and on/off ratio compared to devices without TMA treatment. The data suggest that trace coverages of oxides and other adsorbate dopants (e.g., water) have a strong impact on electrical transport within these QD films. The demonstration of TMA passivation in these studies highlights the importance of developing passivation techniques to improve the design of QD solids for eventual integration into electronic devices and shows that an order of magnitude improvement in QD device performance can be obtained by effectively passivating these trace defect states.

2.6 Acknowledgements

This work was supported by the UC Office of the President under the UC Laboratory Fees Research Program Collaborative Research and Training Award LFR-17-477148. This research used resources of the Advanced Light Source, which is a DOE Office of Science User Facility under contract no. DE-AC02-05CH11231.

Chapter 2, in part or in full, is a reprint of the material as it appears in Applied Surface Science. S. T. Ueda, I. Kwak, A. Abelson, S. Wolf, C. Qian, M. Law, and A. C. Kummel, ”Electronic Passivation of PbSe Quantum Dot Solids by Trimethylaluminum Vapor Dosing”, *Applied Surface Science*, 513, 145812 (2020). The dissertation author was the primary investigator and author of this paper.

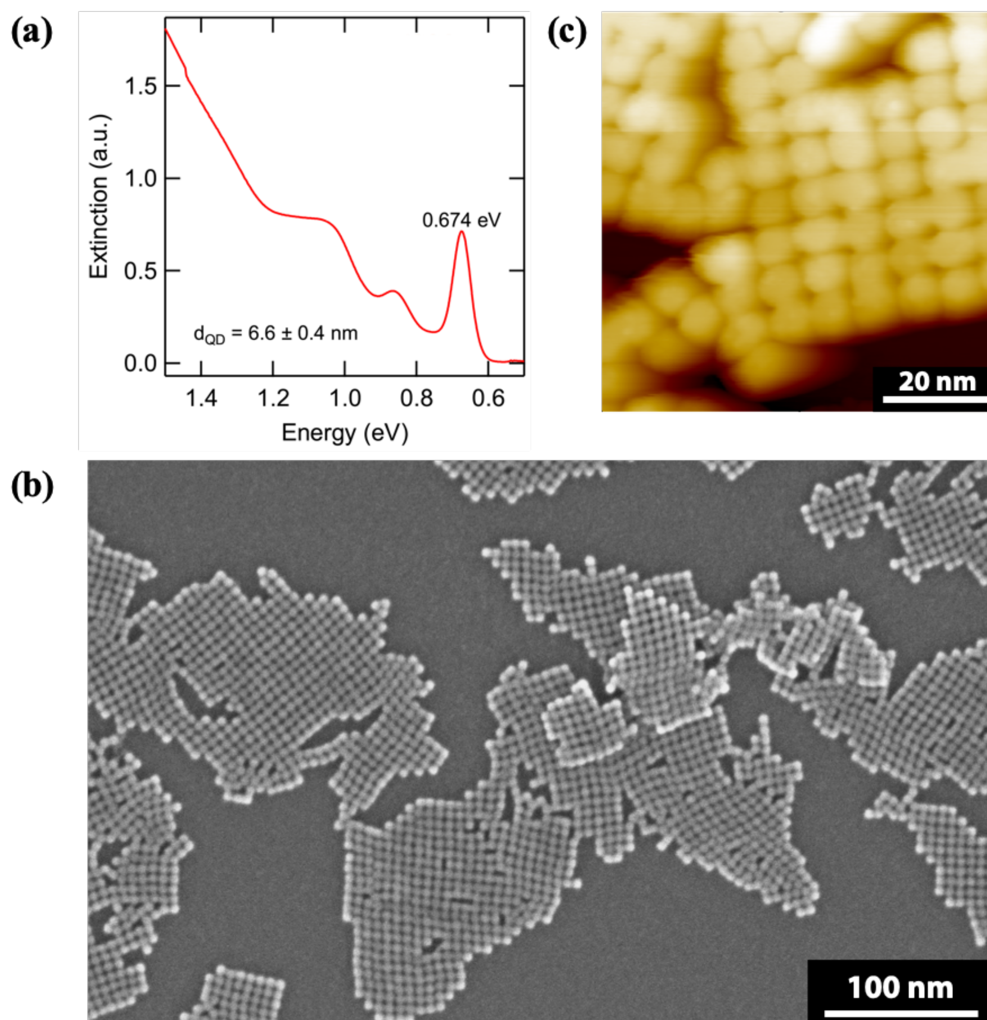

Figure 2.1. The PbSe QD epitaxial superlattices studied by STM. (a) Optical extinction spectrum of the PbSe QDs dispersed in tetrachloroethylene. (b) Representative SEM image of 2D epi-SL grains on HOPG. (c) Corresponding STM topography image.

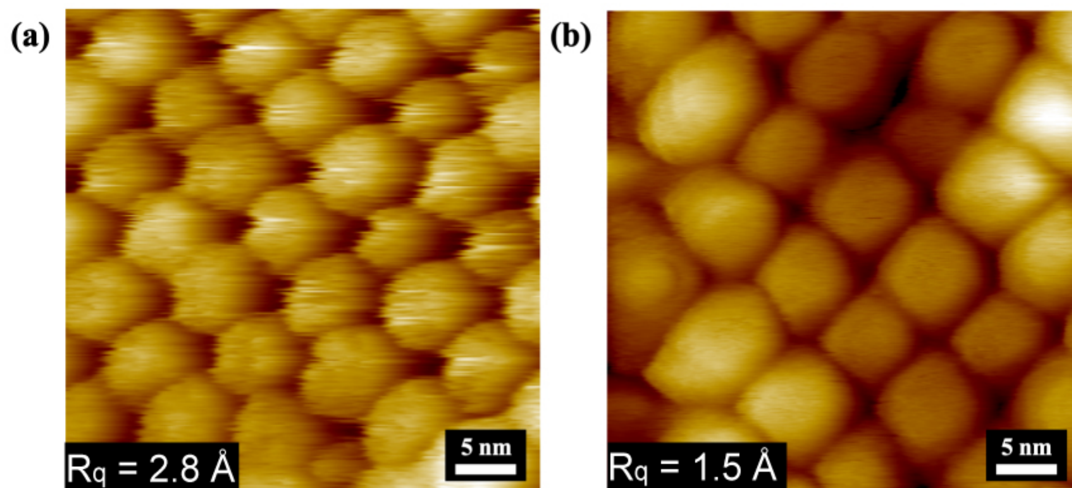

Figure 2.2. Effect of TMA dosing on STM image quality. STM images acquired at 100 K in constant current mode (I = 0.03 nA) with a tip bias of +2 V (a) before and (b) after TMA dosing (2×10^6 L in high vacuum) and their corresponding RMS roughness values (R_q). TMA dosing improves imaging, consistent with the immobilization or removal of loosely-bound adsorbates that interfere with the STM tip.

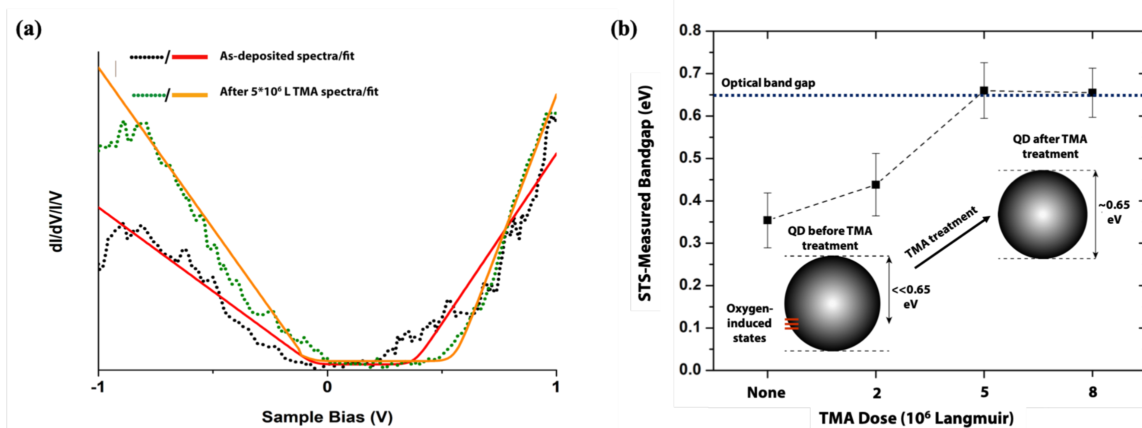

Figure 2.3. Effect of TMA dosing on QD band gap. (a) Representative ST spectra (dashed lines) and fits (solid lines) for a PbSe QD before (red) and after (orange) a 5×10^6 L dose of TMA. (b) Before TMA dosing, the STS-measured band gap of QDs in monolayer epi-SLs is only 0.35 ± 0.07 eV (avg ± 1 SD), much smaller than the optical band gap of the QD films (~0.65 eV). The band gap increases with increasing TMA dose until it saturates at 0.65 ± 0.06 eV, close to the value of the optical band gap. This behavior is consistent with the passivation of gap states by TMA.

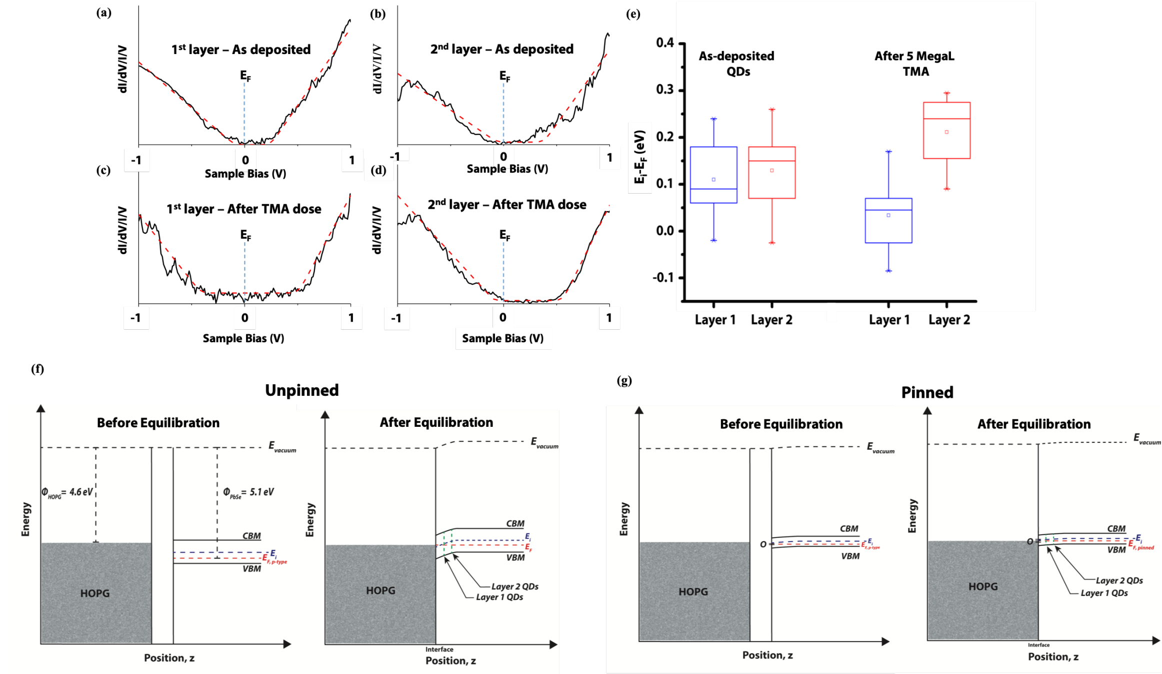

Figure 2.4. Effect of TMA dosing on the Fermi level of QDs in the first and second QD monolayers. (a,b) Typical STS data (solid black lines) and fits [23-24] (dashed red lines) of TMA-treated QDs in the (a) first and (b) second QD monolayers on the HOPG substrate. The Fermi level of QDs in the first monolayer (Layer 1) is located near the middle of the band gap, while the Fermi level of QDs in the second monolayer (Layer 2) is significantly closer to the valence band edge (*p*-type). **(c,d)** Typical STS data (black) and fits (red) for QDs before TMA treatment, showing that QDs in the two layers have similar Fermi levels close to the valence band edge (*p*-type). **(e)** The relative Fermi level (E_i-E_F) of QDs in the two layers before and after TMA dosing. Each line in the boxplot represents a quartile, with the middle line representing the data median. The small square denotes the average of the dataset while the whiskers denote the full data range. **(f,g)** Schematic band diagrams of the HOPG-QD system (f) with and (g) without TMA dosing. With dosing, QD surface states are passivated and the Fermi level is unpinned, resulting in downward band bending in the QD film after equilibration with HOPG and Fermi level positons near mid gap for QDs in the first monolayer and closer to the valence band edge for QDs in the second monolayer. Without dosing, QD surface states pin the Fermi level near the valence band edge, yielding very similar Fermi level positions for QDs in the two monolayers after equilibration with HOPG.

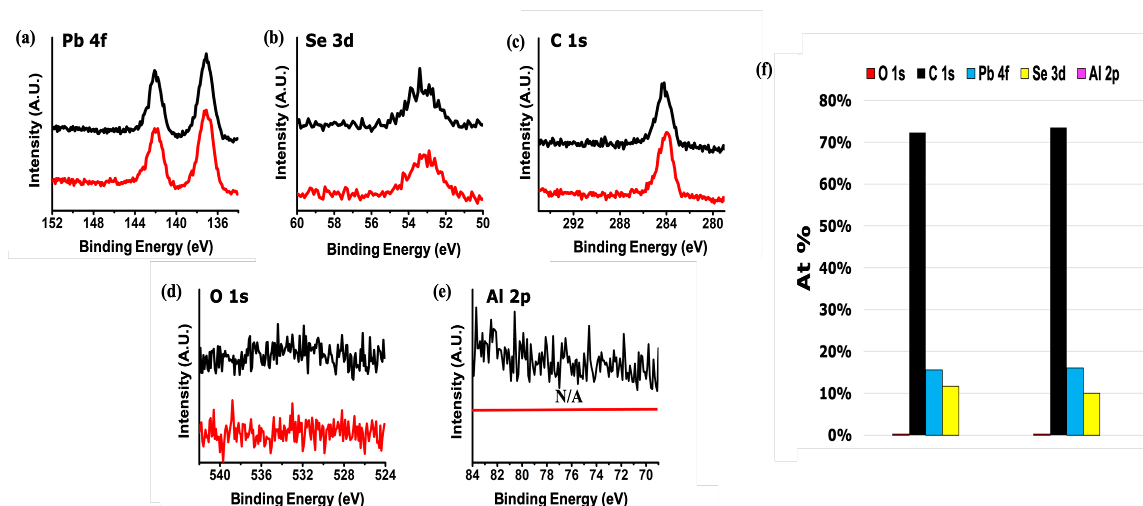

Figure 2.5. XP spectra before and after TMA dosing. (a-e) High-resolution XP spectra of (a) Pb 4f, (b) Se 3d, (c) Al 2p, (d) O 1s, and (e) C 1s before (red) and after (black) TMA dosing (10^7 L). Al and O are below XPS detection limits, demonstrating that nearly all of the QD surface sites are unreactive towards TMA. Pb and Se show no evidence for oxide formation. (f) Sample surface composition before and after TMA dosing.

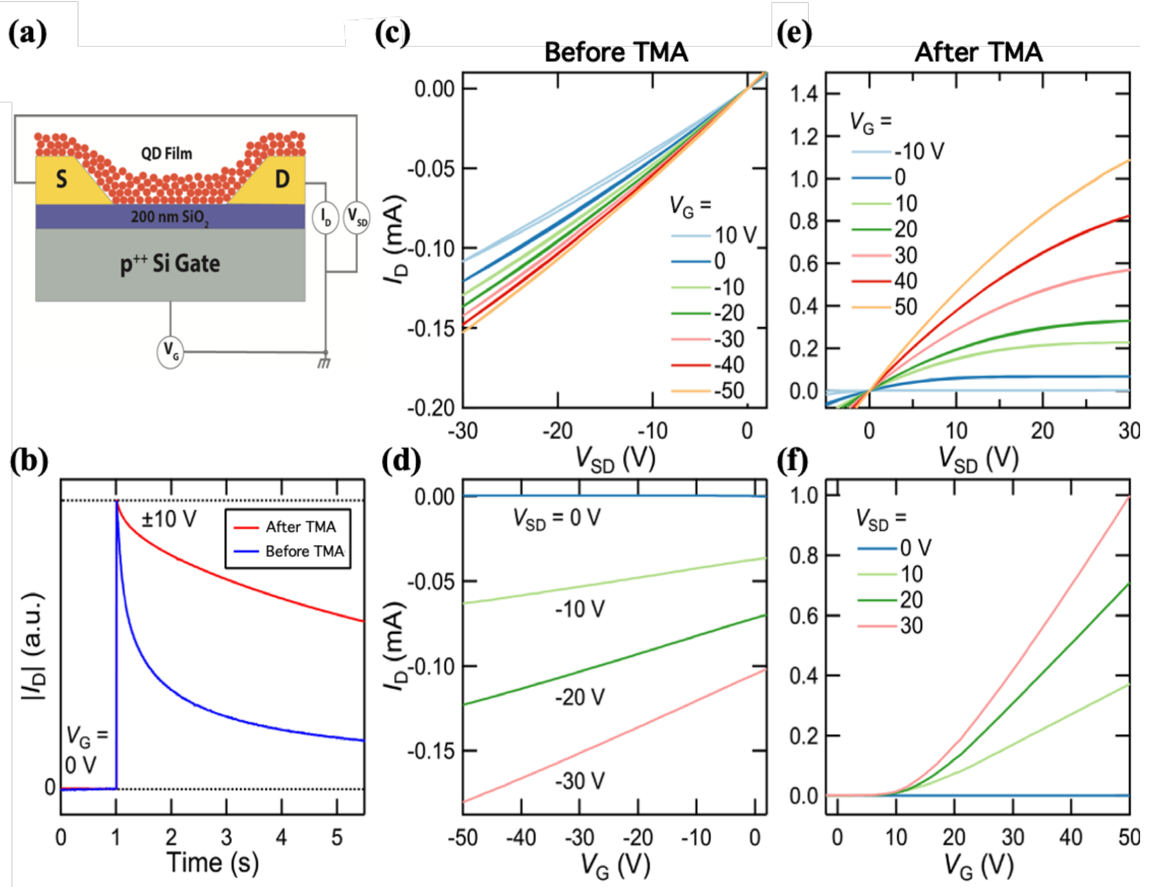

Figure 2.6. Impact of TMA dosing on charge transport in QD field-effect transistors. (a) Schematic of the FET geometry. (b) Normalized drain current for a FET before and after TMA dosing. The applied source-drain bias was -10 V before dosing and +10 V after dosing. The data were normalized to equalize the change in drain current induced by a ±10 V gate bias (negative before dosing and positive after dosing). (c) Output and (d) transfer curves for the FET before TMA dosing. (e) Output and (f) transfer curves immediately after exposure to TMA.

2.7 References

[1] P.V. Kamat, Quantum dot solar cells. Semiconductor nanocrystals as light harvesters, J. Phys. Chem. C (2008), https://doi.org/10.1021/jp806791s.

[2] A.J. Nozik, M.C. Beard, J.M. Luther, M. Law, R.J. Ellingson, J.C. Johnson, Semiconductor quantum dots and quantum dot arrays and applications of multiple exciton generation to third-generation photovoltaic solar cells, Chem. Rev. (2010), https://doi.org/10.1021/cr900289f.

[3] A.G. Midgett, J.M. Luther, J.T. Stewart, D.K. Smith, L.A. Padilha, V.I. Klimov, A.J. Nozik, M.C. Beard, Size and composition dependent multiple exciton generation efficiency in PbS, PbSe, and PbSxSe1-x alloyed quantum dots, Nano Lett. (2013), https://doi.org/10.1021/nl4009748.

[4] M.C. Beard, A.G. Midgett, M.C. Hanna, J.M. Luther, B.K. Hughes, A.J. Nozik, Comparing multiple exciton generation in quantum dots to impact ionization in bulk semiconductors: implications for enhancement of solar energy conversion, Nano Lett. (2010), https://doi.org/10.1021/nl101490z.

[5] R.D. Schaller, V.I. Klimov, High efficiency carrier multiplication in PbSe nanocrystals: implications for solar energy conversion, Phys. Rev. Lett. (2004), https://doi.org/10.1103/PhysRevLett. 92.186601.

[6] R.J. Ellingson, M.C. Beard, J.C. Johnson, P. Yu, O.I. Micic, A.J. Nozik, A. Shabaev, A.L. Efros, Highly efficient multiple exciton generation in colloidal PbSe and PbS quantum dots, Nano Lett. (2005), https://doi.org/10.1021/nl0502672.

[7] J. Minbiao, P. Sungnam, S.T. Connor, T. Mokari, C. Yi, K.J. Gaffney, Efficient multiple exciton generation observed in colloidal PbSe quantum dots with temporally and spectrally resolved intraband excitation, Nano Lett. (2009), https://doi.org/10.1021/nl900103f.

[8] M.T. Trinh, A.J. Houtepen, J.M. Schins, J. Piris, L.D.A. Siebbeles, Nature of the second optical transition in PbSe nanocrystals, Nano Lett. (2008), https://doi.org/10.1021/nl8010963.

[9] J.E. Murphy, M.C. Beard, A.G. Norman, S.P. Ahrenkiel, J.C. Johnson, P. Yu, O.I. Mićić, R.J. Ellingson, A.J. Nozik, PbTe colloidal nanocrystals: synthesis, characterization, and multiple exciton generation, J. Am. Chem. Soc. (2006), https://doi.org/10.1021/ja0574973.

[10] E. Kalesaki, W.H. Evers, G. Allan, D. Vanmaekelbergh, C. Delerue, Electronic structure of atomically coherent square semiconductor superlattices with dimensionality

below two, Phys. Rev. B – Condens. Matter Mater. Phys. (2013), https://doi.org/10.1103/PhysRevB.88.115431.

[11] C.R. Kagan, C.B. Murray, Charge transport in strongly coupled quantum dot solids, Nat. Nanotechnol. (2015), https://doi.org/10.1038/nnano.2015.247.

[12] A.T. Fafarman, W.K. Koh, B.T. Diroll, D.K. Kim, D.K. Ko, S.J. Oh, X. Ye, V. DoanNguyen, M.R. Crump, D.C. Reifsnyder, et al., Thiocyanate-capped nanocrystal colloids: vibrational reporter of surface chemistry and solution-based route to enhanced coupling in nanocrystal solids, J. Am. Chem. Soc. (2011), https://doi.org/ 10.1021/ja206303g.

[13] J. Tang, K.W. Kemp, S. Hoogland, K.S. Jeong, H. Liu, L. Levina, M. Furukawa, X. Wang, R. Debnath, D. Cha, et al., Colloidal-quantum-dot photovoltaics using atomic-ligand passivation, Nat. Mater. (2011), https://doi.org/10.1038/nmat3118.

[14] H. Zhang, B. Hu, L. Sun, R. Hovden, F.W. Wise, D.A. Muller, R.D. Robinson, Surfactant ligand removal and rational fabrication of inorganically connected quantum dots, Nano Lett. (2011), https://doi.org/10.1021/nl202892p.

[15] A. Abelson, C. Qian, T. Salk, Z. Luan, K. Fu, J.-G. Zheng, J.L. Wardini, M. Law, Collective topo-epitaxy in the self-assembly of a 3D quantum dot superlattice, Nat. Mater. (2020), https://doi.org/10.1038/s41563-019-0485-2.

[16] Y. Liu, J. Tolentino, M. Gibbs, R. Ihly, C.L. Perkins, Y. Liu, N. Crawford, J.C. Hemminger, M. Law, PbSe quantum dot field-effect transistors with air-stable electron mobilities above 7 cm2 V-1 s -1, Nano Lett. (2013), https://doi.org/10.1021/ nl304753n.

[17] K.S. Leschkies, M.S. Kang, E.S. Aydil, D.J. Norris, Influence of atmospheric gases on the electrical properties of PbSe quantum-dot films, J. Phys. Chem. C (2010), https://doi.org/10.1021/jp101695s.

[18] M. Sykora, A.Y. Koposov, J.A. McGuire, R.K. Schulze, O. Tretiak, J.M. Pietryga, V.I. Klimov, Effect of air exposure on surface properties, electronic structure, and carrier relaxation in PbSe nanocrystals, ACS Nano (2010), https://doi.org/10. 1021/nn100131w.

[19] J. Tang, L. Brzozowski, D.A.R. Barkhouse, X. Wang, R. Debnath, R. Wolowiec, E. Palmiano, L. Levina, A.G. Pattantyus-Abraham, D. Jamakosmanovic, et al., Quantum Dot Photovoltaics in the Extreme Quantum Confinement Regime: The Surface-Chemical Origins of Exceptional Air- and Light-Stability, ACS Nano, 2010, https://doi.org/10.1021/nn901564q.

[20] I. Moreels, K. Lambert, D. De Muynck, F. Vanhaecke, D. Poelman, J.C. Martins, G. Allan, Z. Hens, Composition and size-dependent extinction coefficient of colloidal PbSe quantum dots, Chem. Mater. (2007), https://doi.org/10.1021/ cm071410q.

[21] Ilavsky, J. Nika, Software for two-dimensional data reduction, J. Appl. Crystallogr. (2012), https://doi.org/10.1107/s0021889812004037.

[22] S.R. Kline, Reduction and analysis of SANS and USANS data using IGOR pro, J. Appl. Crystallogr. (2006), https://doi.org/10.1107/s0021889806035059.

[23] R.M. Feenstra, Tunneling spectroscopy of the (110) surface of direct-Gap III-V semiconductors, Phys. Rev. B (1994), https://doi.org/10.1103/PhysRevB.50.4561.

[24] R.M. Feenstra, J.Y. Lee, M.H. Kang, G. Meyer, K.H. Rieder, Band Gap of the Ge (111) c (2×8) Surface by Scanning Tunneling Spectroscopy, Phys. Rev. B - Condens. Matter Mater. Phys. (2006), https://doi.org/10.1103/PhysRevB.73. 035310.

[25] J.M. Luther, M. Law, M.C. Beard, Q. Song, M.O. Reese, R.J. Ellingson, A.J. Nozik, Schottky solar cells based on colloidal nanocrystal films, Nano Lett. (2008), https:// doi.org/10.1021/nl802476m.

[26] Y. Wang, X. Peng, A. Abelson, P. Xiao, C. Qian, L. Yu, C. Ophus, P. Ercius, L.- W. Wang, M. Law, H. Zheng, Dynamic deformability of individual PbSe nanocrystals during superlattice phase transitions, Sci. Adv. 5 (2019) (6), https://doi.org/10. 1126/sciadv.aaw5623.

[27] W.J. Baumgardner, K. Whitham, T. Hanrath, Confined-but-connected quantum solids via controlled ligand displacement, Nano Lett. (2013), https://doi.org/10. 1021/nl401298s.

[28] W.H. Evers, B. Goris, S. Bals, M. Casavola, J. De Graaf, R.Van Roij, M. Dijkstra, D. Vanmaekelbergh, Low-dimensional semiconductor superlattices formed by geometric control over nanocrystal attachment, Nano Lett. (2013), https://doi.org/10. 1021/nl303322k.

[29] T. Tiedje, J. Varon, H. Deckman, J. Stokes, Tip contamination effects in ambient pressure scanning tunneling microscopy imaging of graphite, J. Vac. Sci. Technol. A Vacuum, Surfaces, Film. (2002), https://doi.org/10.1116/1.575418.

[30] D.V. Talapin, C.B. Murray, Applied Physics: PbSe Nanocrystal Solids for n- and pChannel Thin Film Field-Effect Transistors, Science (80-.) (2005), https://doi.org/ 10.1126/science.1116703.

[31] D. Kim, D.H. Kim, J.H. Lee, J.C. Grossman, Impact of stoichiometry on the electronic structure of PbS quantum dots, Phys. Rev. Lett. (2013), https://doi.org/10. 1103/PhysRevLett. 110.196802.

[32] T. Kaufman-Osborn, E.A. Chagarov, A.C. Kummel, Atomic imaging and modeling of H2O2(g) surface passivation, functionalization, and atomic layer deposition nucleation on the Ge(100) surface, J. Chem. Phys. (2014), https://doi.org/10.1063/1. 4878496.

[33] D. Zhitomirsky, I.J. Kramer, A.J. Labelle, A. Fischer, R. Debnath, J. Pan, O.M. Bakr, E.H. Sargent, Colloidal quantum dot photovoltaics: the effect of polydispersity, Nano Lett. (2012), https://doi.org/10.1021/nl2041589.

[34] P. Nagpal, V.I. Klimov, Role of mid-gap states in charge transport and photoconductivity in semiconductor nanocrystal films, Nat. Commun. (2011), https:// doi.org/10.1038/ncomms1492.

[35] D. Zhitomirsky, M. Furukawa, J. Tang, P. Stadler, S. Hoogland, O. Voznyy, H. Liu, E.H. Sargent, n-Type colloidal-quantum-dot solids for photovoltaics, Adv. Mater. (2012), https://doi.org/10.1002/adma.201202825.

[36] G. Konstantatos, L. Levina, A. Fischer, E.H. Sargent, Engineering the temporal response of photoconductive photodetectors via selective introduction of surface trap states, Nano Lett. (2008), https://doi.org/10.1021/nl080373e.

[37] M.H. Zarghami, Y. Liu, M. Gibbs, E. Gebremichael, C. Webster, M. Law, p-Type PbSe and PbS quantum dot solids prepared with short-chain acids and diacids, ACS Nano (2010), https://doi.org/10.1021/nn100339b.

[38] N. Zhao, T.P. Osedach, L.Y. Chang, S.M. Geyer, D. Wanger, M.T. Binda, A.C. Arango, M.G. Bawendi, V. Bulovic, Colloidal PbS quantum dot solar cells with high fill factor, ACS Nano (2010), https://doi.org/10.1021/nn100129j.

[39] Y. Zhang, D. Zherebetskyy, N.D. Bronstein, S. Barja, L. Lichtenstein, A.P. Alivisatos, L.W. Wang, M. Salmeron, Molecular oxygen induced in-gap states in PbS quantum dots, ACS Nano (2015), https://doi.org/10.1021/acsnano.5b04677.

[40] J.M. Luther, M. Law, Q. Song, C.L. Perkins, M.C. Beard, A.J. Nozik, Structural, Optical, and electrical properties of self-assembled films of PbSe nanocrystals treated with 1,2-ethanedithiol, ACS Nano (2008), https://doi.org/10.1021/ nn7003348.

[41] S.J. Oh, D.K. Kim, C.E.R. Kagan, Remote doping and schottky barrier formation in strongly quantum confined single PbSe nanowire field-effect transistors, ACS Nano (2012), https://doi.org/10.1021/nn3009382.

[42] C. Adelmann, D. Cuypers, M. Tallarida, L.N.J. Rodriguez, A. De Clercq, D. Friedrich, T. Conard, A. Delabie, J.W. Seo, J.P. Locquet, et al., Surface chemistry and interface formation during the atomic layer deposition of alumina from trimethylaluminum and water on indium phosphide, Chem. Mater. (2013), https://doi.org/10.1021/cm304070h.

[43] V.V. Tomaev, L.L. Makarov, P.A. Tikhonov, A.A. Solomennikov, Oxidation kinetics of lead selenide, Glas. Phys. Chem. (2004), https://doi.org/10.1023/B:GPAC.0000038709.80613.51.

[44] C. Gautier, M. Cambon-Muller, M. Averous, Study of PbSe layer oxidation and oxide dissolution, Appl. Surf. Sci. (1999), https://doi.org/10.1016/S0169-4332(98)00606-0.

[45] M. Tallarida, C. Adelmann, A. Delabie, S. Van Elshocht, M. Caymax, D. Schmeisser, Surface chemistry and fermi level movement during the self-cleaning of GaAs by trimethyl-aluminum, Appl. Phys. Lett. (2011), https://doi.org/10.1063/1.3615784.

[46] C.L. Hinkle, A.M. Sonnet, E.M. Vogel, S. McDonnell, G.J. Hughes, M. Milojevic, B. Lee, F.S. Aguirre-Tostado, K.J. Choi, H.C. Kim, J. Kim, R.M. Wallace, GaAs interfacial self-cleaning by atomic layer deposition, Appl. Phys. Lett. (2008), https://doi.org/10.1063/1.2883956.

[47] H.D. Trinh, E.Y. Chang, Y.Y. Wong, C.C. Yu, C.Y. Chang, Y.C. Lin, H.Q. Nguyen, B.T. Tran, Effects of wet chemical and trimethyl aluminum treatments on the interface properties in atomic layer deposition of Al2O3 on InAs, Jpn. J. Appl. Phys. (2010), https://doi.org/10.1143/JJAP.49.111201.

[48] M. Milojevic, R. Contreras-Guerrero, M. Lopez-Lopez, J. Kim, R.M. Wallace, Characterization of the "Clean-up" of the Oxidized Ge(100) Surface by Atomic Layer Deposition, Appl. Phys. Lett. (2009), https://doi.org/10.1063/1.3268449.

[49] T.P. Osedach, N. Zhao, T.L. Andrew, P.R. Brown, D.D. Wanger, D.B. Strasfeld, L.Y. Chang, M.G. Bawendi, V. Bulović, Bias-stress effect in 1,2-ethanedithiol-treated PbS quantum dot field-effect transistors, ACS Nano (2012), https://doi.org/10.1021/nn3008788.

[50] Y. Liu, M. Gibbs, J. Puthussery, S. Gaik, R. Ihly, H.W. Hillhouse, M. Law, Dependence of carrier mobility on nanocrystal size and ligand length in PbSe nanocrystal solids, Nano Lett. (2010), https://doi.org/10.1021/nl101284k.

[51] J.H. Choi, A.T. Fafarman, S.J. Oh, D.K. Ko, D.K. Kim, B.T. Diroll, S. Muramoto, J.G. Gillen, C.B. Murray, C.R. Kagan, Bandlike transport in strongly coupled and doped quantum dot solids: a route to high-performance thin-film electronics, Nano Lett. (2012), https://doi.org/10.1021/nl301104z.

[52] D. Zherebetskyy, M. Scheele, Y. Zhang, N. Bronstein, C. Thompson, D. Britt, M. Salmeron, P. Alivisatos, L.W. Wang, Hydroxylation of the surface of PbS nanocrystals passivated with oleic acid, Science (80-.) (2014), https://doi.org/10.1126/ science.1252727.

Chapter 3

Tris(dimethylamido)aluminum(III) and N_2H_4: Ideal precursors for the low-temperature deposition of large grain, oriented c-axis AlN on Si via atomic layer annealing

3.1 Abstract

The low-temperature (≤ 400 ºC) deposition of polycrystalline AlN films on silicon is demonstrated by atomic layer annealing (ALA) using either trimethyl aluminum (TMA) and anhydrous hydrazine (N_2H_4) or tris(dimethylamido) aluminum (TDMAA) and anhydrous N_2H_4 with an argon plasma treatment utilizing a DC bias to tune the ion energy. Using TDMAA and N_2H_4, high-quality AlN films are deposited with large grain size and low oxygen/carbon contamination which can be used as a templating layer for further high-speed AlN film growth via sputtering. The deposition of high-quality AlN films deposited by ALA are successfully used as templates for sputtered AlN resulting in a >2x improvement in average grain size when compared to an analogous amorphous template layer.

3.2 Introduction

High-quality, large-grained AlN films are of interest for use in a number of applications such as for heat spreading layers [1-3] or as a buffer/templating layer for further film growth [4-8], with deposition on Si being often required. As the typical deposition temperature for high-quality crystalline AlN is usually in excess of 800 ºC [9-10], there is a large amount of thermal strain in the films and it is advantageous to develop processes to lower the deposition temperature so that it is compatible with back end of line

(BEOL) processing. Plasma enhanced atomic layer deposition (PEALD) of AlN has been extensively studied as a potential solution [11-18]; however, this process relies on a reactive nitrogen-containing plasma (N_2 or NH_3) which can affect the stoichiometry of the deposited films and imposes a limit to the tunability of ion energy/momentum, which is key to depositing large grain crystalline films [19-23].

In this work, the low-temperature ($\leq$ 400 ^{o}C) deposition of polycrystalline AlN films on Si(111) is demonstrated by atomic layer annealing (ALA) which is a variant of atomic layer deposition (ALD) that utilizes a third pulse of low-energy inert gas ions in addition to the usual metal and co-reactant pulses (See Fig. 3.1) [24]. Using this technique, the stoichiometries of the films are determined by the thermal reaction of the metal and co-reactant while the crystallinity is controlled by the plasma treatment with a non-reactive gas.

Using trimethyl aluminum (TMA) or tris(dimethylamido) aluminum (TDMAA) with the highly reactive nitrogen-containing precursor hydrazine (N_2H_4), AlN can be deposited at ~200 ^{o}C [25-26]; however, these films are amorphous. Using TDMAA with N_2H_4 or NH_3 at temperatures $\geq$350 ^{o}C, polycrystalline films can be deposited in a purely thermal process; however, the reported grain sizes are small (<5 nm) or there is a mixture of polycrystalline and amorphous phases [27-28]. ALA has been used to deposit crystalline films such as AlN [24, 29] and GaN [30] on a near lattice-matched substrate (sapphire) at low temperatures, but a N_2/H_2 plasma was used and the effects of substrate biasing were not explored.

In the present study of AlN ALA on Si (111) (a non-lattice matched substrate), two metal precursors (TMA and TDMAA) were compared using ultra-high purity anhydrous

N_2H_4 as a co-reactant and argon ions with tuned energy for the third pulse. It was found that ALA deposition using TDMAA as the Al precursor resulted in high-quality AlN films with large grain size (>9 nm) and low C/O contamination (< 2 at. %) whereas films deposited using TMA had much higher carbon content (>5 at. %), owing to its thermal instability at 400 °C [31-33]. Transmission electron micrographs for a 10 nm ALA AlN film grown using TDMAA and N_2H_4 show vertical grain structure with grains spanning the entire thickness of the film. As heat spreading layers often need to be in excess of > 250 nm thick in order to be relevant for use in high volume manufacturing, it was also demonstrated that ALA-deposited films successfully enhance the grain size of a thick sputtered AlN film by acting as a template layer.

3.3 Experimental

3.3.1 Materials

Si (111) substrate wafers (Phosphorous, n-type) with a resistivity of 1-20 ohm-cm were purchased from Waferworld. Acetone (99.5+%), methanol (99.5+%), and deionized (DI) water (99.5%+) were purchased from Fisher Scientific. Hydrofluoric (HF) acid (48%) was purchased from VWR and diluted down to 2% with DI water before use. Ar (99.999%) was purchased from Praxair and purified using an Entegris Gatekeeper gas purifier before being used as both the plasma gas as well as the precursor carrier gas. TMA (98+%) was purchased from Strem chemicals. Ammonia (99.999%) was purchased from Praxair. TDMAA was supplied by EMD performance materials. BRUTE anhydrous hydrazine (30 ppb vapor phase H_2O) was supplied by Rasirc, Inc.

3.3.2 Sample Preparation

Si samples were first degreased using 10 s rinses in acetone, methanol, and DI water. Following the degrease, native oxides were removed via a cyclic HF clean consisting of 1 min immersions in HF and DI water for 2.5 cycles. Immediately following the clean, the samples were loaded onto a sample holder and pumped down to a pressure of $<2*10^{-6}$ Torr before loading into the deposition chamber.

3.3.3 AlN Deposition

The ALA deposition was conducted in a home-built chamber (wall temp = 90 °C) with a base pressure $<1x10^{-6}$ Torr and consisted of a home-built reactor pumped by a dry pump (Edwards EPX 500NE) protected by a liquid nitrogen cold trap and stainless steel mesh particle trap. The stage allows for sample biasing and consists of an electrically isolated copper block heated by a cartridge heater. Dosing was performed using pneumatically actuated diaphragm valves and although self-saturating behavior was not observed, pulse times were optimized for growth rates of ~0.9 Å/cycle in order to keep the film thickness between each ALA treatment constant. TDMAA was dosed using a bottle temperature of 105 °C while all other precursors were kept at room temperature. TMA was dosed under its own vapor pressure while both the TDMAA and N_2H_4 cylinders were charged with Ar carrier gas in order to deliver the precursors to the sample. For larger exposures, multiple doses of TDMAA and N_2H_4 were used in order to recharge the cylinders with Ar carrier gas and deliver the precursors. As TMA has sufficient vapor pressure, this technique was not needed and longer pulse times could be used. Gas flows

were controlled by mass flow controllers and fed into a RF remote plasma source (PIE Scientific) with a quartz plasma tube mounted above the chamber. ALA used a 20 s treatment each cycle using Ar gas at a pressure of 5 mTorr at a power of 75 W with a pulsed stage bias of -25 VDC. For bilayer samples (ALA AlN + sputtered AlN), following ALA deposition, samples were transported *in vacuo* to an attached sputter chamber (based pressure ~$2x10^{-6}$ Torr) where AlN was deposited using a Torus Magkeeper sputter cathode (Kurt Lesker) using a 2 inch diameter Al target and 100% N_2 gas at a pressure of 3 mTorr and 300W of RF power. Amorphous AlN layers were deposited under similar sputtering conditions but at a pressure of 30 mTorr.

3.3.4 X-ray Photoelectron Spectroscopy (XPS)

Samples were transferred from the deposition chamber to the UHV analysis (Omicron VT, base pressure $5x10^{-9}$ Torr) chamber *in vacuo*. High resolution XP spectra were acquired on the as-deposited samples without any surface treatment (e.g., Ar sputtering or UHV annealing) using a Mg Kα source ($h\nu$ = 1253.6 eV) and DESA 150 electron analyzer (Staib Instruments) at a collection angle of 45° relative to the surface normal using a step width of 0.1 eV. Analysis of the XPS data was performed in CasaXPS v2.3 using Shirley background subtraction and Schofield photoionization cross sectional relative sensitivity factors.

3.3.5 Structural Analysis

Ex situ grazing incidence x-ray diffractometry (GIXRD) and x-ray reflectometry (XRR) were carried out on a diffractometer (Smartlab, Rigaku) using a Cu Kα source

(λ=0.154 nm) operating at 40kV. Simulation and fitting of the XRR data was carried out using the Smartlab Studio software suite (Rigaku). Cross-sectional transmission electron microscopy (TEM) was used to evaluate the fine grain structure of the deposited films and was performed at Applied Materials.

3.4 Results and Discussion

3.4.1 Comparison of TMA and TDMAA at 225 °C

Two Al precursors (TMA and TDMAA) were first benchmarked at 225 ^{o}C. Using a purely thermal process, sequential doses of either 400 ms TMA and 2x100 ms pulses of N_2H_4 with 5 s purge times or 2x300 ms TDMAA with a 4 s purge and 100 ms N_2H_4 with an 8 s purge were used. For ALA samples, each cycle also included a 20 s Ar plasma treatment with the stage biased at -25 VDC. This cyclic process was repeated in order to deposit films ~40 nm in thickness. As can be seen in Fig. 3.2, the thermal process for both TDMAA and TMA results in films of similar purity; however, the ALA process removes much more carbonaceous contamination in the case of TDMAA, possibly due to the lack of any direct Al-C bonding in TDMAA. Although the XPS data appear to indicate slightly Al-rich films, it is noted that spectra collected on crystalline AlN films also have Al:N ratios ranging from ~1.05-1.1:1; therefore, it is hypothesized that this artifact arises from the higher kinetic energy of the Al 2p electron as compared to the N 1s electron as any thin overlayer would lead to higher attenuation of the N 1s signal and lead to a high Al:N ratio when measured by XPS. Chemical shift data collected from high resolution XP spectra are consistent with the formation of stoichiometric AlN and also demonstrate the beneficial effect of ALA on C/O contamination in these films.

3.4.2 Structural Analysis of Films Deposited at 225 °C

Structural analysis of these films via XRD show that all samples had at best marginal crystallinity regardless of process (Fig. 3.3). Though small XRD peaks corresponding to AlN (002) were observed for the ALA process, the density of these films as measured by XRR was found to be 2.5 and 2.8 g/cm^3 for the TMA ALA and TDMAA sample, respectively, which is >15% lower than the bulk value for crystalline AlN and likely indicates large percentages of the films are amorphous. Previous studies on PEALD deposited AlN using low (<100 W) power also note that at lower temperatures, crystallization of the film does not occur at T <300 °C [17] and that either higher deposition temperature or increased plasma power were needed to form crystalline films [15, 34-35], with these results being in rough agreement with the work of Bosund et al. [17] after taking into account these thinner films of ~40 nm will display poorer crystallinity due to higher dislocation density close to the interface.

3.4.3 Comparison of TMA and TDMAA at 400 °C

Since thermal AlN films are typically seen to crystallize at temperatures of 350-375 °C, the same two precursors were then compared at 400 °C deposition temperature to elucidate the impact of the ALA process on weakly crystalline films. As all temperatures at which thermal crystallization of AlN would occur are higher than the decomposition temperature of TMA [31-33, 36, 37], the highest temperature allowed for BEOL processing (~400 °C) was chosen. Owing to the improved reactivities of the precursors at 400 °C, precursor pulses were modified to 35 ms TMA with a 10 s purge and 100 ms N_2H_4 with an

8 s purge or 150 ms TDMAA with a 4 s purge and 100 ms N_2H_4 with an 8 s purge. ALA samples received the same 20 s Ar plasma treatment with the stage biased at -25 VDC used previously. Due to the thermal decomposition of TMA at 400 °C, the lowest growth rate attainable was 1.8 Å/cycle. As it can be seen in Fig 3.4, films grown using TDMAA have lower impurity concentration for both the thermal as well as ALA processes and the ALA TDMAA process has lower impurities than the thermal ALD TDMAA process. Although the precise mechanism for the reduction in impurity content from ALA is not known, it is hypothesized that this effect is due to either a gentle sputtering process that removes surface oxides and carbonaceous species (including unreacted ligands) or that the enhanced density as a result of the ALA prevents the incorporation of these impurities into the film. It is noted that at 400 °C using TMA, the ALA process actually increases the carbon content in the AlN films. This is likely linked to the thermal instability of TMA at high temperatures which may result in the generation of carbon-containing species such as gaseous methyl radicals that the plasma then imbeds in the AlN films. In contrast, because TDMAA does not contain any C-Al bonds and has high thermally stability at 400 °C, the resulting AlN films do not contain high levels of carbon [38-39]. NH_3 was tested as an alternative co-reactant for the ALA process at 400°C; however, owing to the lower reactivity as compared to N_2H_4, growth rate was reduced and O contamination was increased. From the high-resolution carbon XP spectra (Fig. 3.4b), it is seen that for the TDMAA ALA process, aliphatic carbon is reduced to below detection limits while the remaining component just above detection limits is likely surface bound dimethylamide. Especially noteworthy is the ALA process with TDMAA achieves extremely low impurity concentration (< 2 at. % C/O) even without sputtering into the bulk of the film.

3.4.4 Structural Analysis of Films Deposited at 400 °C

Subsequent XRD analysis (Fig. 3.5) confirms that the TDMAA ALA process leads to the highest quality films of oriented c-axis AlN. The film densities of the ALA samples were measured by XRR to be 3.0 g/cm^3 and 3.3 g/cm^3 for the TMA ALA and TDMAA sample, respectively, which indicates that the elevated carbon content in the TMA ALA sample likely prevented crystallization while the TDMAA ALA sample has a density within 1% of bulk crystalline AlN and a full width at half the maximum intensity (FWHM) value of 0.95°, which corresponds to a crystallite size of ~9.2 nm by the Scherer equation [40].

3.4.5 Templated Growth of Sputtered AlN

In order to demonstrate the effect of these ALA-deposited layers, sputter deposition was identified as one method capable of quickly depositing crystalline AlN at temperatures compatible with BEOL processing. Sputter-deposited AlN films can contain large amounts of compressive strain[41] when deposited on Si (111) and so it is necessary to use a buffer layer in order to avoid cracking or flaking of the deposited film. Thin, 25 nm ALA AlN films grown using TDMAA were subsequently deposited for use as templates for the growth of 290 nm of sputter deposited AlN and compared against a buffer layer composed of 25 nm of amorphous AlN. As it can be seen in Fig 3.6, the template layers deposited via ALA on a non-lattice-matched substrate Si (111) are smooth and contain grains >10 nm wide that span the entire thickness of the film.

The initial growth stages of sputtering are an essentially stochastic process when performed on a non-lattice matched substrate. This results in multiple grain orientations or the formation of dislocations/defects that reduce the average grain size of the sputtered material. Due to the ALA template acting as a lattice matched substrate, it was expected that sputtered films grown on the ALA layers would have larger average grain size with and have stronger (002) preferential orientation as compared to the amorphous AlN buffer layers. As it can be seen in Fig 3.7, XRD data show that sputtered AlN grown on amorphous AlN is polycrystalline (002)/(103) with no preferential orientation while the AlN grown on the ALA AlN template is highly textured (002). TEM data of the sample grown on ALA AlN (Fig. 3.8) show the grain structure of the sputtered layer originating from the ALA layer which then serves to template the columnar growth of the film. When comparing the FWHM of the (002) peak, the sample grown on amorphous AlN has a much larger FWHM (1.09°) as compared to the sample grown on ALA AlN (0.45°) which corresponds to an increase in average grain size from 8 nm to 19.4 nm by using the ALA template layer.

3.5 Conclusion

In summary, it is demonstrated that precursor selection is key for developing processes for the low temperature deposition of oriented crystalline materials on non-lattice matched substrates such as Si (111). It is shown that even at the relatively modest temperature of 400 °C, commonly used precursors such as TMA do not possess the thermal stability needed in order to deposit high quality crystalline films and that there exists a need for non-intuitive precursors such as TDMAA and N_2H_4. Through the selection of precursors that are thermally stable, yet highly reactive, oriented c-axis AlN films are able

to be grown on Si via bias enhanced ALA. These films have an average grain size >9 nm and are successfully shown to template the growth of sputtered AlN which results in a 2x increase in the average grain size (19 nm) as compared to an AlN film sputtered on amorphous AlN (8 nm). As this process does not require a lattice-matched substrate and is BEOL compatible, it is relevant for a wide range of applications ranging from buffer layer deposition to CMOS/RF heat spreaders.

3.6 Acknowledgements

This work was supported in part by the Applications and Systems-Driven Center for Energy Efficient Integrated Nano Technologies (ASCENT), one of six centers in the Joint University Microelectronics Program (JUMP), an SRC program sponsored by the Defense Advanced Research Program Agency (DARPA). The authors would also like to gratefully acknowledge support from Applied Materials, Rasirc, and EMD.

Chapter 3, in part or in full, is a reprint of the material as it appears in Applied Surface Science. S. T. Ueda, A. McLeod, D. Alvarez, D. Moser, R. Kanjolia, M. Moinpour, J. Woodruff, and A. C. Kummel, "Tris(dimethylamido)aluminum(III) and N_2H_4: Ideal precursors for the deposition of large grain, oriented c-axis AlN on Si via atomic layer annealing", *Applied Surface Science*, 554, 149656 (2021). The dissertation author was the primary investigator and author of this paper.

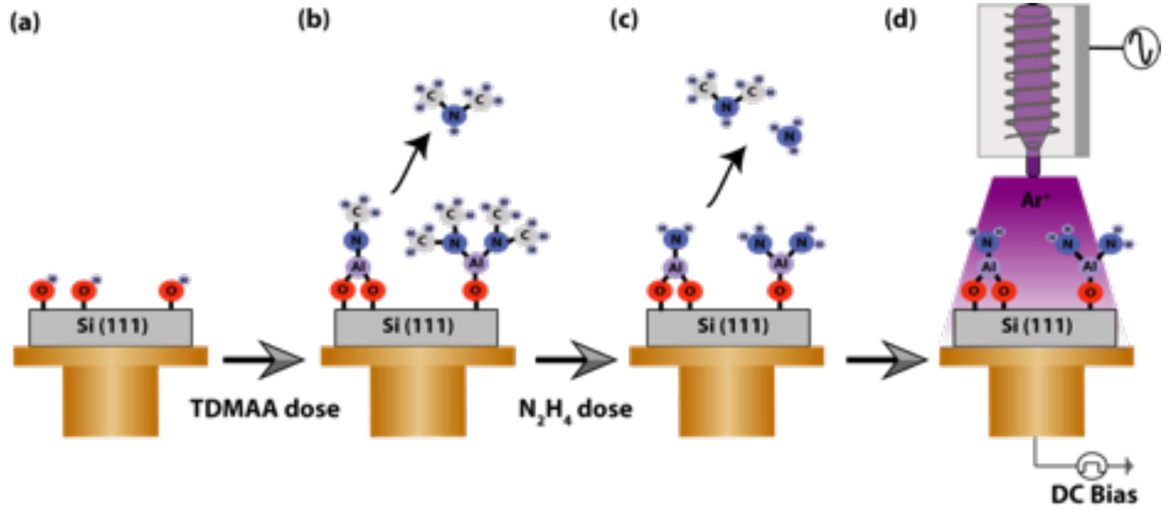

Figure 3.1. Schematic Diagram of ALA AlN. (a) Beginning with a hydroxyl terminated Si wafer, (b) the TDMAA is introduced leaving the surface terminated in aluminum dimethylamide. (c) Introduction of N_2H_4 removes the surface bound dimethylamide as dimethylamine gas. (d) The final step in the ALA process consists of low energy ion bombardment which helps to induce surface mobility and crystalize the film. This 3-step process can be repeated any number of times to achieve the desired thickness.

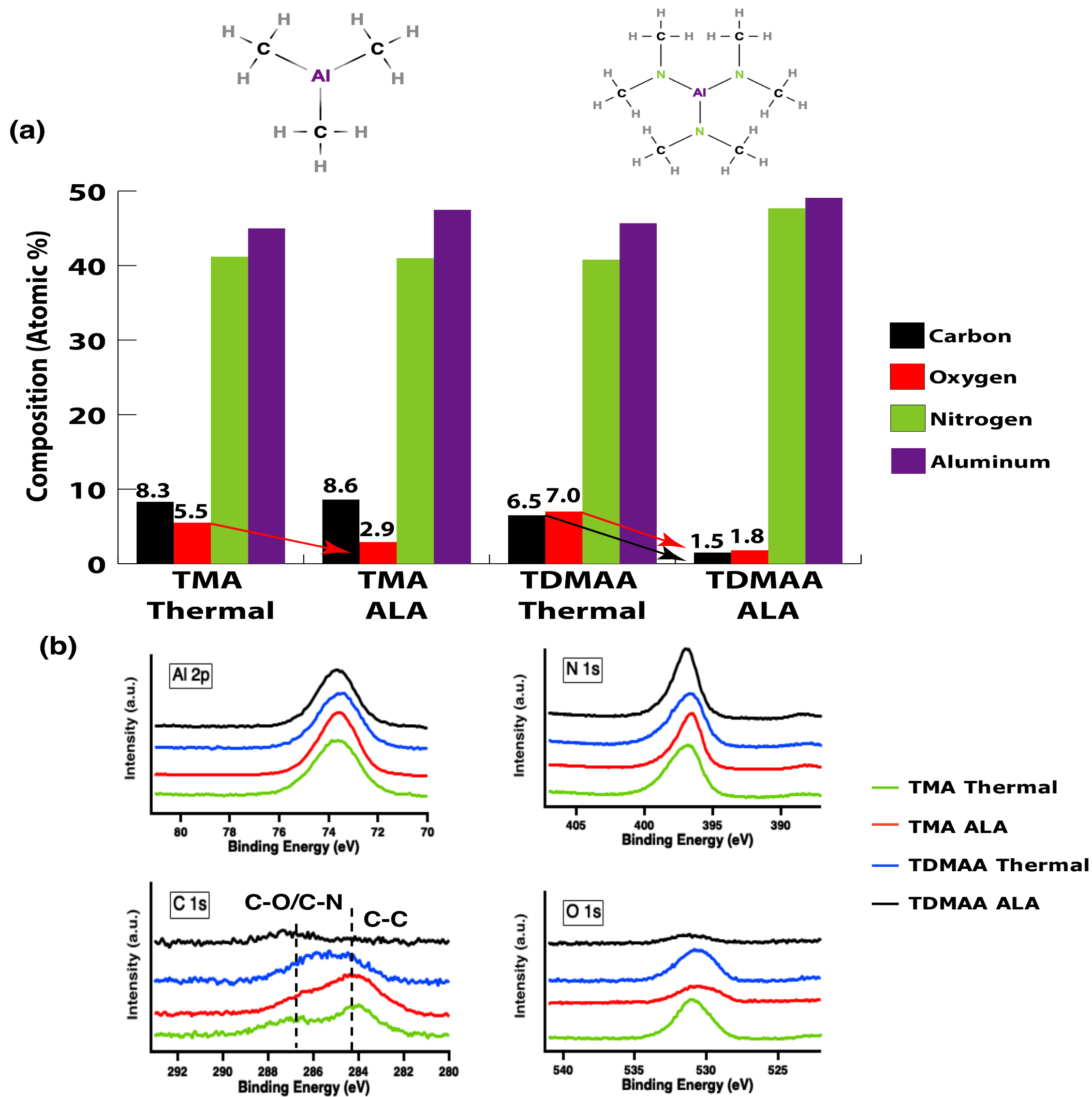

Figure 3.2. XPS Chemical Composition Data for both Thermal and ALA Processes using TMA and TDMAA at 225 °C. (a) The chemical compositions for the thermal process using TMA or TDMAA are very similar, with the ALA process resulting in the removal of unwanted C/O, especially when using TDMAA. Molecular schematics of the two precursors are shown (as monomers) above the corresponding XPS data. (b) High resolution XP spectra show chemical shift consistent with stochiometric AlN formation and the effect of ALA on the C/O contamination.

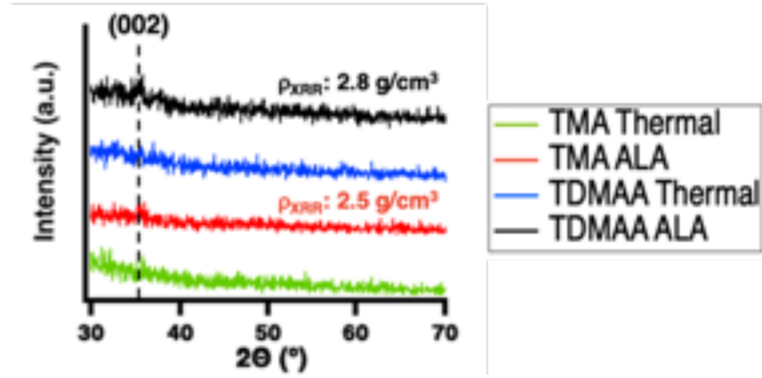

Figure 3.3. XRD Data for both Thermal and ALA Processes using TMA and TDMAA at 225 °C. The deposited films are either amorphous or nanocrystalline. Note that even when small crystalline peaks are observed for the ALA process, density via XRR is much lower than bulk crystalline AlN.

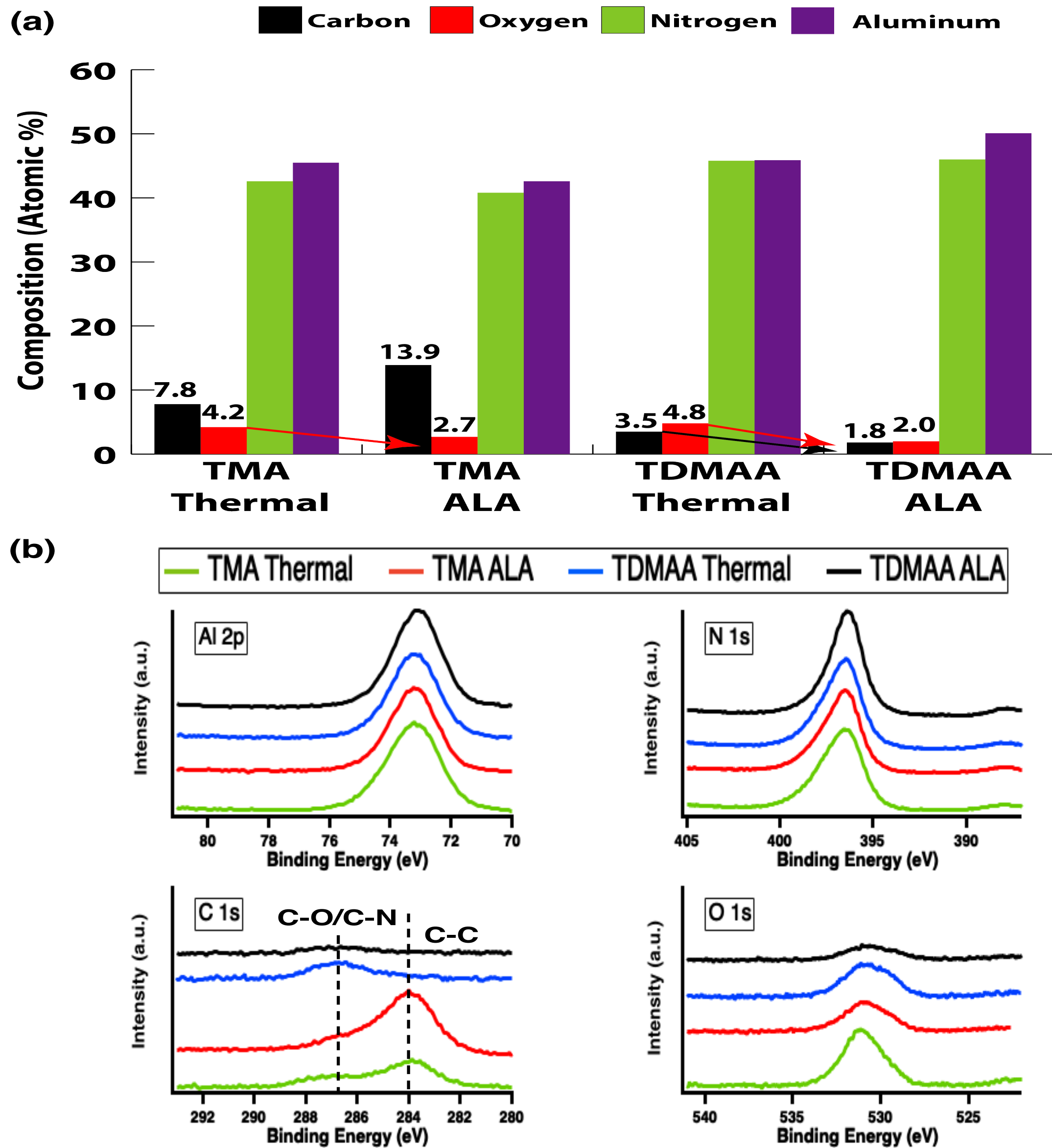

Figure 3.4. XPS Chemical Composition Data for both Thermal and ALA Processes using TMA and TDMAA at 400 °C. (a) At 400 °C substrate temperature, films grown using TDMAA have lower impurity content, with the ALA films containing the lowest impurity content of < 2 at. % C/O. (b) High resolution XP spectra show chemical shift consistent with stoichiometric AlN formation and the effect of ALA on the C/O contamination.

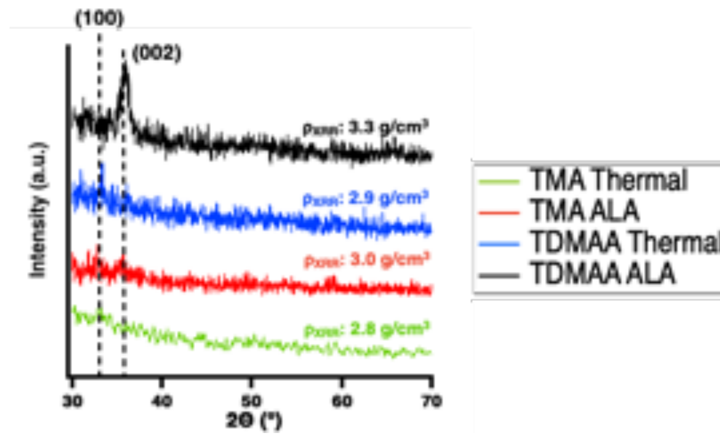

Figure 3.5. XRD Data for both Thermal and ALA Processes using TMA and TDMAA at 400 °C. Films grown using TDMAA ALA display oriented (002) growth as compared to the other processes which are predominantly (100) oriented, mixed phase, or amorphous. Note bulk-like AlN density is only achieved for TDMAA ALA.

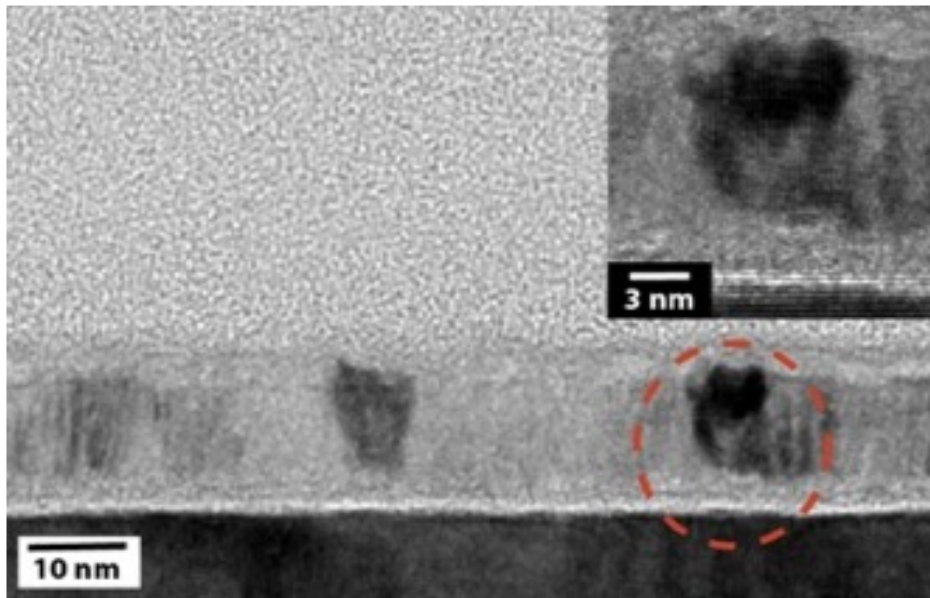

Figure 3.6. Bright Field TEM Image of a 10 nm ALA AlN layer. Template layers are smooth by TEM and have large grains that extend through the entire thickness of the film (inset: high resolution TEM showing the lattice fringes).

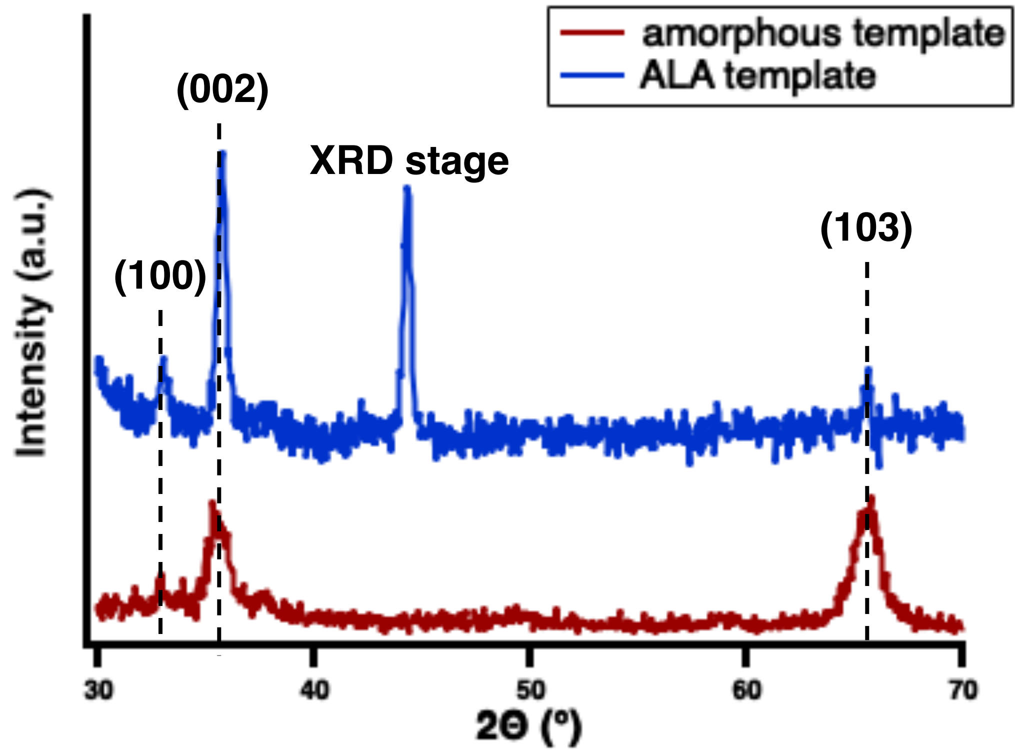

Figure 3.7. XRD data comparing AlN films using a 25 nm amorphous AlN buffer layer with a 25 nm ALA AlN buffer layer. Replacing the amorphous AlN buffer layer with ALA AlN results in 2.5x improvement in grain size for equivalent thickness of sputtered material.

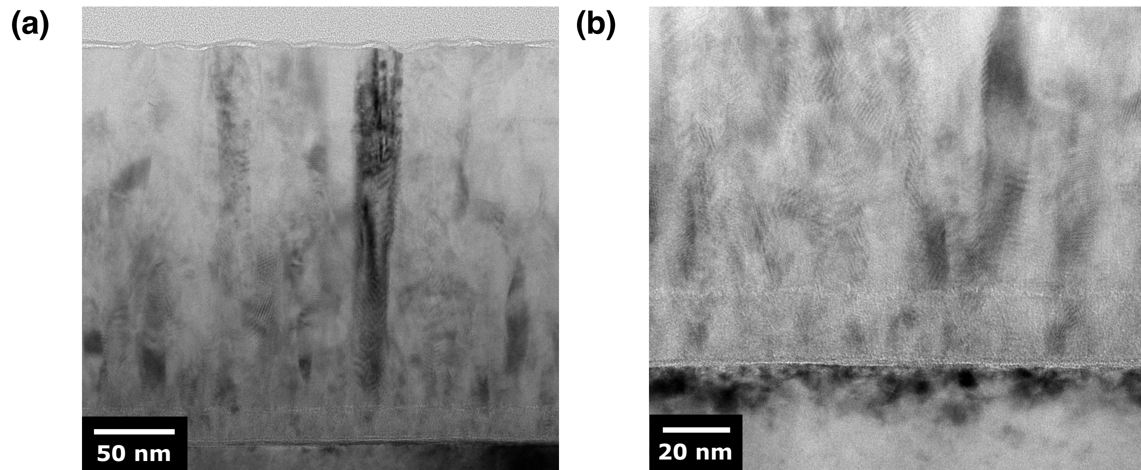

Figure 3.8. Bright Field TEM Image of a 25 nm ALA AlN templating the growth of 290 nm sputtered AlN. (a) Columnar grains are observed that extend from the top of the film to the substrate. (b) The sputtered grain structure originates from the template layer and then grows vertically.

3.7 References

[1] Xu, R. L.; Munõz Rojo, M.; Islam, S. M.; Sood, A.; Vareskic, B.; Katre, A.; Mingo, N.; Goodson, K. E.; Xing, H. G.; Jena, D.; et al. Thermal Conductivity of Crystalline AlN and the Influence of Atomic-Scale Defects. *J. Appl. Phys.* **2019**. https://doi.org/10.1063/1.5097172.

[2] Heo, Y. J.; Kim, H. T.; Kim, K. J.; Nahm, S.; Yoon, Y. J.; Kim, J. Enhanced Heat Transfer by Room Temperature Deposition of AlN Film on Aluminum for a Light Emitting Diode Package. In *Applied Thermal Engineering*; 2013. https://doi.org/10.1016/j.applthermaleng.2012.07.024.

[3] La Spina, L.; Iborra, E.; Schellevis, H.; Clement, M.; Olivares, J.; Nanver, L. K. Aluminum Nitride for Heatspreading in RF IC's. *Solid. State. Electron.* **2008**. https://doi.org/10.1016/j.sse.2008.04.009.

[4] Lu, H.; Schaff, W. J.; Hwang, J.; Wu, H.; Koley, G.; Eastman, L. F. Effect of an AlN Buffer Layer on the Epitaxial Growth of InN by Molecular-Beam Epitaxy. *Appl. Phys. Lett.* **2001**. https://doi.org/10.1063/1.1402649.

[5] Ponce, F. A.; Major, J. S.; Plano, W. E.; Welch, D. F. Crystalline Structure of AlGaN Epitaxy on Sapphire Using AlN Buffer Layers. *Appl. Phys. Lett.* **1994**. https://doi.org/10.1063/1.112724.

[6] Amano, H.; Akasaki, I.; Hiramatsu, K.; Koide, N.; Sawaki, N. Effects of the Buffer Layer in Metalorganic Vapour Phase Epitaxy of GaN on Sapphire Substrate. *Thin Solid Films* **1988**. https://doi.org/10.1016/0040-6090(88)90458-0.

[7] Kuznia, J. N.; Khan, M. A.; Olson, D. T.; Kaplan, R.; Freitas, J. Influence of Buffer Layers on the Deposition of High Quality Single Crystal GaN over Sapphire Substrates. *J. Appl. Phys.* **1993**. https://doi.org/10.1063/1.354069.

[8] Shiino, T.; Shiba, S.; Sakai, N.; Yamakura, T.; Jiang, L.; Uzawa, Y.; Maezawa, H.; Yamamoto, S. Improvement of the Critical Temperature of Superconducting NbTiN and NbN Thin Films Using the AlN Buffer Layer. *Supercond. Sci. Technol.* **2010**. https://doi.org/10.1088/0953-2048/23/4/045004.

[9] Chen, Y.; Song, H.; Li, D.; Sun, X.; Jiang, H.; Li, Z.; Miao, G.; Zhang, Z.; Zhou, Y. Influence of the Growth Temperature of AlN Nucleation Layer on AlN Template Grown by High-Temperature MOCVD. *Mater. Lett.* **2014**. https://doi.org/10.1016/j.matlet.2013.09.096.

[10] Kakanakova-Georgieva, A.; Nilsson, D.; Janzén, E. High-Quality AlN Layers Grown by Hot-Wall MOCVD at Reduced Temperatures. *J. Cryst. Growth* **2012**. https://doi.org/10.1016/j.jcrysgro.2011.10.052.

[11] Van Bui, H.; Wiggers, F. B.; Gupta, A.; Nguyen, M. D.; Aarnink, A. A. I.; de Jong, M. P.; Kovalgin, A. Y. Initial Growth, Refractive Index, and Crystallinity of Thermal and Plasma-Enhanced Atomic Layer Deposition AlN Films. *J. Vac. Sci. Technol. A Vacuum, Surfaces, Film.* **2015**. https://doi.org/10.1116/1.4898434.

[12] Sippola, P.; Pyymaki Perros, A.; Ylivaara, O. M. E.; Ronkainen, H.; Julin, J.; Liu, X.; Sajavaara, T.; Etula, J.; Lipsanen, H.; Puurunen, R. L. Comparison of Mechanical Properties and Composition of Magnetron Sputter and Plasma Enhanced Atomic Layer Deposition Aluminum Nitride Films. *J. Vac. Sci. Technol. A* **2018**. https://doi.org/10.1116/1.5038856.

[13] Banerjee, S.; Aarnink, A. A. I.; van de Kruijs, R.; Kovalgin, A. Y.; Schmitz, J. PEALD AlN: Controlling Growth and Film Crystallinity. *Phys. Status Solidi Curr. Top. Solid State Phys.* **2015**. https://doi.org/10.1002/pssc.201510039.

[14] Alevli, M.; Ozgit, C.; Donmez, I.; Biyikli, N. Structural Properties of AlN Films Deposited by Plasma-Enhanced Atomic Layer Deposition at Different Growth Temperatures. *Phys. Status Solidi Appl. Mater. Sci.* **2012**. https://doi.org/10.1002/pssa.201127430.

[15] Tarala, V.; Ambartsumov, M.; Altakhov, A.; Martens, V.; Shevchenko, M. Growing C-Axis Oriented Aluminum Nitride Films by Plasma-Enhanced Atomic Layer Deposition at Low Temperatures. *J. Cryst. Growth* **2016**. https://doi.org/10.1016/j.jcrysgro.2016.10.015.

[16] Motamedi, P.; Cadien, K. Structural and Optical Characterization of Low-Temperature ALD Crystalline AlN. *J. Cryst. Growth* **2015**. https://doi.org/10.1016/j.jcrysgro.2015.04.009.

[17] Bosund, M.; Sajavaara, T.; Laitinen, M.; Huhtio, T.; Putkonen, M.; Airaksinen, V. M.; Lipsanen, H. Properties of AlN Grown by Plasma Enhanced Atomic Layer Deposition. *Appl. Surf. Sci.* **2011**. https://doi.org/10.1016/j.apsusc.2011.04.037.

[18] Liu, S.; Peng, M.; Hou, C.; He, Y.; Li, M.; Zheng, X. PEALD-Grown Crystalline AlN Films on Si (100) with Sharp Interface and Good Uniformity. *Nanoscale Res. Lett.* **2017**. https://doi.org/10.1186/s11671-017-2049-1.

[19] Wang, J.; Maier, R. L.; Schreiber, H. Crystal Phase Transition of HfO2 Films Evaporated by Plasma-Ion-Assisted Deposition. *Appl. Opt.* **2008**. https://doi.org/10.1364/AO.47.00C189.

[20] Park, J.-S.; Park, H.-S.; Kang, S.-W. Plasma-Enhanced Atomic Layer Deposition of Ta-N Thin Films. *J. Electrochem. Soc.* **2002**. https://doi.org/10.1149/1.1423642.

[21] Profijt, H. B.; Van De Sanden, M. C. M.; Kessels, W. M. M. Substrate Biasing during Plasma-Assisted ALD for Crystalline Phase-Control of TiO 2 Thin Films. *Electrochem. Solid-State Lett.* **2012**. https://doi.org/10.1149/2.024202esl.

[22] Profijt, H. B.; van de Sanden, M. C. M.; Kessels, W. M. M. Substrate-Biasing during Plasma-Assisted Atomic Layer Deposition to Tailor Metal-Oxide Thin Film Growth. *J. Vac. Sci. Technol. A Vacuum, Surfaces, Film.* **2013**. https://doi.org/10.1116/1.4756906.

[23] Faraz, T.; Knoops, H. C. M.; Verheijen, M. A.; Van Helvoirt, C. A. A.; Karwal, S.; Sharma, A.; Beladiya, V.; Szeghalmi, A.; Hausmann, D. M.; Henri, J.; et al. Tuning Material Properties of Oxides and Nitrides by Substrate Biasing during Plasma-Enhanced Atomic Layer Deposition on Planar and 3D Substrate Topographies. *ACS Appl. Mater. Interfaces* **2018**. https://doi.org/10.1021/acsami.8b00183.

[24] Shih, H. Y.; Lee, W. H.; Kao, W. C.; Chuang, Y. C.; Lin, R. M.; Lin, H. C.; Shiojiri, M.; Chen, M. J. Low-Temperature Atomic Layer Epitaxy of AlN Ultrathin Films by Layer-by-Layer, in-Situ Atomic Layer Annealing. *Sci. Rep.* **2017**. https://doi.org/10.1038/srep39717.

[25] Mizuta, M.; Fujieda, S.; Matsumoto, Y.; Kawamura, T. Low Temperature Growth of Gan and Ain on Gaas Utilizing Metalorganics and Hydrazine. *Jpn. J. Appl. Phys.* **1986**. https://doi.org/10.1143/JJAP.25.L945.

[26] Jung, Y. C.; Hwang, S. M.; Le, D. N.; Kondusamy, A. L. N.; Mohan, J.; Kim, S. W.; Kim, J. H.; Lucero, A. T.; Ravichandran, A.; Kim, H. S.; et al. Low Temperature Thermal Atomic Layer Deposition of Aluminum Nitride Using Hydrazine as the Nitrogen Source. *Materials (Basel).* **2020**. https://doi.org/10.3390/ma13153387.

[27] Gordon, R. G.; Riaz, U.; Hoffman, D. M. Chemical Vapor Deposition of Aluminum Nitride Thin Films. *J. Mater. Res.* **1992**, *7* (7), 1679–1684. https://doi.org/10.1557/JMR.1992.1679.

[28] Abdulagatov, A. I.; Ramazanov, S. M.; Dallaev, R. S.; Murliev, E. K.; Palchaev, D. K.; Rabadanov, M. K.; Abdulagatov, I. M. Atomic Layer Deposition of Aluminum Nitride Using Tris(Diethylamido)Aluminum and Hydrazine or Ammonia. *Russ. Microelectron.* **2018**. https://doi.org/10.1134/S1063739718020026.

[29] Kao, W. C.; Lee, W. H.; Yi, S. H.; Shen, T. H.; Lin, H. C.; Chen, M. J. AlN Epitaxy on SiC by Low-Temperature Atomic Layer Deposition: Via Layer-by-Layer, in Situ Atomic Layer Annealing. *RSC Adv.* **2019**.

https://doi.org/10.1039/c9ra00008a.

[30] Lee, W. H.; Yin, Y. T.; Cheng, P. H.; Shyue, J. J.; Shiojiri, M.; Lin, H. C.; Chen, M. J. Nanoscale GaN Epilayer Grown by Atomic Layer Annealing and Epitaxy at Low Temperature. *ACS Sustain. Chem. Eng.* **2019**. https://doi.org/10.1021/acssuschemeng.8b03982.

[31] Yamashita, S.; Watanuki, K.; Ishii, H.; Shiba, Y.; Kitano, M.; Shirai, Y.; Sugawa, S.; Ohmi, T. Dependence of the Decomposition of Trimethylaluminum on Oxygen Concentration. *J. Electrochem. Soc.* **2011**. https://doi.org/10.1149/1.3517080.

[32] Riihelä, D.; Ritala, M.; Matero, R.; Leskelä, M.; Jokinen, J.; Haussalo, P. Low Temperature Deposition of AlN Films by an Alternate Supply of Trimethyl Aluminum and Ammonia. *Chem. Vap. Depos.* **1996**. https://doi.org/10.1002/cvde.19960020612.

[33] Rouf, P.; Sukkaew, P.; Ojamäe, L.; Pedersen, H. Reduction of Carbon Impurities in Aluminum Nitride from Time-Resolved Chemical Vapor Deposition Using Trimethylaluminum. *J. Phys. Chem. C* **2020**. https://doi.org/10.1021/acs.jpcc.0c01724.

[34] Ozgit, C.; Donmez, I.; Alevli, M.; Biyikli, N. Self-Limiting Low-Temperature Growth of Crystalline AlN Thin Films by Plasma-Enhanced Atomic Layer Deposition. *Thin Solid Films* **2012**. https://doi.org/10.1016/j.tsf.2011.11.081.

[35] Ozgit-Akgun, C.; Goldenberg, E.; Okyay, A. K.; Biyikli, N. Hollow Cathode Plasma-Assisted Atomic Layer Deposition of Crystalline AlN, GaN and AlxGa1-XN Thin Films at Low Temperatures. *J. Mater. Chem. C* **2014**. https://doi.org/10.1039/c3tc32418d.

[36] Squire, D. W. Mechanistic Studies of the Decomposition of Trimethylaluminum on Heated Surfaces. *J. Vac. Sci. Technol. B Microelectron. Nanom. Struct.* **1985**. https://doi.org/10.1116/1.582976.

[37] Gow, T. R.; Lin, R.; Cadwell, L. A.; Lee, F.; Backman, A. L.; Masel, R. I. Decomposition of Trimethylaluminum on Si(100). *Chem. Mater.* **1989**. https://doi.org/10.1021/cm00004a006.

[38] Abdulagatov, A. I.; Amashaev, R. R.; Ashurbekova, K. N.; Ashurbekova, K. N.; Rabadanov, M. K.; Abdulagatov, I. M. Atomic Layer Deposition of Aluminum Nitride and Oxynitride on Silicon Using Tris(Dimethylamido)Aluminum, Ammonia, and Water. *Russ. J. Gen. Chem.* **2018**. https://doi.org/10.1134/S1070363218080236.

[39] Buttera, S. C.; Mandia, D. J.; Barry, S. T. Tris(Dimethylamido)Aluminum(III): An Overlooked Atomic Layer Deposition Precursor. *J. Vac. Sci. Technol. A Vacuum, Surfaces, Film.* **2017**. https://doi.org/10.1116/1.4972469.

[40] Scherrer, P. Bestimmung Der Größe Und Der Inneren Struktur von Kolloidteilchen Mittels Röntgenstrahlen. *Nachrichten von der Gesellschaft der Wissenschaften zu Göttingen, Math. Klasse* **1918**.

[41] Kusaka, K.; Taniguchi, D.; Hanabusa, T.; Tominaga, K. Effect of Sputtering Gas Pressure and Nitrogen Concentration on Crystal Orientation and Residual Stress in Sputtered AlN Films. *Vacuum* **2002**. https://doi.org/10.1016/S0042-207X(02)00168-9.

Chapter 4

Experimental and Theoretical Determination of the Role of Ions in Atomic Layer Annealing

4.1 Abstract

The atomic layer annealing process has recently shown promise as a technique for the deposition of crystalline materials that can be performed at the low temperatures of atomic layer deposition. However, the precise mechanism of the crystallization effect has not yet been thoroughly explored. In the present study, independent experimental control of ion momentum and energy are used in conjunction with molecular dynamics simulations to elucidate the role of ions in atomic layer annealing. It was found that via a momentum transfer process, ions can displace surface atoms during initial contact and that they later induce a short-lived local heating phenomenon in the first few atomic layers, resulting in enhanced crystallinity. It was seen that by using a heavier gas such as Kr, energy transfer to the growth surface could be improved, enabling the repair of a wider variety of crystallographic defects.

4.2 Introduction

As microelectronic devices continue to be scaled to the atomic limit, pressure on extant deposition methods such as physical vapor deposition (PVD) or conventional chemical vapor deposition (CVD) continues to increase. Increasingly stringent demands on thickness control, conformality, and material quality on the 3-dimensional (3-D) architectures commonly being used in these devices has led to the greater adoption of atomic layer deposition (ALD) for thin film growth, especially in the low thermal budget

back end of line [1-6]. Despite the numerous advantages of ALD, ALD-deposited films are often amorphous due to the moderate deposition temperatures (typically < 400 °C) required to minimize precursor decomposition/desorption and to stay in the 'ALD window' [4-7].

For many applications (e.g., surface or bulk acoustic wave devices [8-11] or heat spreaders [12-14]), the deposition of crystalline films is required, which has led to the increasing adoption of a variant of ALD known as atomic layer annealing (ALA) as an alternative or supplement to conventional plasma enhanced ALD (PEALD) [7, 15-19]. In the ALA process, either thermal ALD or PEALD is used to deposit the target material and low energy inert gas ions are used to bombard the surface. Using this ABC-type pulse sequence (reactant A, reactant B, and inert ions C), high quality crystalline films can be deposited at low temperatures; however, the precise role of the inert ions in this process has thus far remained unclear.

In the present report, the mechanism of the ALA process is elucidated using AlN as an example material system due to its wide-ranging applications for crystalline films as a heat spreader or piezoelectric material. It was previously reported that ALA strongly relies on a so-called surface heating effect; however, through systematic experimental variation of inert ion mass, plasma delay time, and molecular dynamics (MD) simulations, it is shown that the process is most consistent with a momentum transfer process resulting in effective local thermal excitation leading to surface crystallization (See schematic of ALA AlN process in Fig. 4.1).

4.3 Experimental

4.3.1 Materials

Acetone (99.5 +%), methanol (99.5 +%), and deionized (DI) water (99.5 +%) were purchased from Fisher Scientific. Hydrofluoric (HF) acid (48 %) was purchased from VWR and diluted down to 2 % with DI water before use. Tris(dimethylamido) aluminum (TDMAA) was supplied by EMD performance materials. BRUTE anhydrous hydrazine was supplied by Rasirc, Inc. Ar (99.999 +%) was purchased from Praxair and purified using an Entegris Gatekeeper gas purifier for use as a carrier gas for both TDMAA and hydrazine. Si (111) substrate wafers (Phosphorous, n-type) with a resistivity of 1-20 ohm-cm were purchased from Waferworld. Research grade (99.999 +%) Ne, Ar, and Kr gas purchased from Praxair was used as the plasma gas for the ALA process.

4.3.2 Sample Preparation

Si (111) samples were first degreased using sequential 10 s rinses in acetone, methanol, and DI water. Following this degrease, the native Si oxide was removed via a cyclic HF clean consisting of sequential 1 min immersions in 2 % HF solution and DI water for 2.5 cycles. Immediately following the cyclic HF clean, the samples were loaded onto a molybdenum sample holder and pumped down to a pressure of $< 2*10^{-6}$ Torr before being loaded into the deposition chamber.

4.3.3 AlN Deposition

AlN deposition conditions have been reported elsewhere [19]. Briefly, AlN deposition was conducted in a custom vacuum chamber (wall temp = 90 ºC) with a base

pressure <$1x10^{-6}$ Torr and consisted of a home-built reactor pumped by a dry pump (Edwards EPX 500NE) protected by both a liquid nitrogen cold trap and stainless steel mesh particle trap. The sample stage consisted of a copper block heated externally via a cartridge heater and was electrically isolated to allow for biasing. Dosing was controlled using pneumatically actuated diaphragm valves and although self-saturating behavior was not observed, pulse times (100 ms for TDMAA and 150 ms for N_2H_4) and purge times (8 s for both precursors) were optimized for growth rates of ~0.9 Å/cycle to match typical ALD growth rates. TDMAA was dosed using a bottle temperature of 105 °C while N_2H_4 was kept at room temperature. Both the TDMAA and N_2H_4 cylinders were charged with Ar carrier gas to deliver the precursors to the sample. Gas flows were controlled by mass flow controllers and fed into a RF remote plasma source (PIE Scientific) with a quartz plasma tube mounted above the chamber. ALA treatment time was fixed at 20 s and used either Ne, Ar, or Kr gas at a pressure of 5 mTorr. The power was controlled to keep a constant ion current density of ~0.25 mA/cm^2 (~$1.5*10^{19}$ ions m^{-2} s^{-1}) in all cases.

4.3.4 X-ray Photoelectron Spectroscopy

Chemical composition was determined *in vacuo* using an attached UHV chamber (Omicron VT, base pressure ~$5x10^{-10}$ Torr). High resolution XP spectra were acquired on the as-deposited samples without any surface treatment (e.g., Ar sputtering or UHV annealing) using a Mg Kα source (hv = 1253.6 eV) and DESA 150 electron analyzer (Staib Instruments) at a collection angle of 45° relative to the surface normal using a step width of 0.1 eV. Analysis of the XPS data was performed in CasaXPS v2.3 using Shirley

background subtraction and Scofield photoionization cross sectional relative sensitivity factors.

4.3.5 X-ray Diffraction

Ex situ grazing incidence x-ray diffractometry (GIXRD) was carried out on a Rigaku Smartlab diffractometer using a Cu Kα source (λ=0.154 nm) operating at 40 kV. X-ray reflectivity (XRR) data was collected on the same tool with modeling and fitting conducted using the Smartlab Studio software suite (Rigaku). For consistency, all samples were of approximately the same thickness of ~40 nm as measured by XRR.

4.3.6 Atomic Force Microscopy

Sample topography was determined using a Keysight 5500 scanning probe microscope in tapping mode using, etched Si tips with Al backside coating (Bruker).

4.4 Results and Discussion

4.4.1 Effect of Inert Ion Mass on Atomic Layer Annealing

To determine the effect of ion momentum and energy on the ALA process, various inert gasses were used for the ion treatment step in addition to a controlled DC bias applied to the substrate. By changing the inert gas from Ne (~20 amu) to Ar (~40 amu) or Kr (~80 amu), while maintaining constant ion current density and treatment time, momentum could independently be tuned from energy and flux. If the primary crystallization effect was due to a plasma heating effect, it was expected that the crystallization effect would be

independent of inert ion mass, or as noted in previous reports [16, 20], that heavier ions would reduce the crystalline quality of the film by inducing ion damage [18, 21].

As it can be seen in the GIXRD scans in Fig. 4.2, the full width at half maximum (FWHM) of the AlN (002) GIXRD peaks in general decreased with increasing ion mass, with Kr exhibiting the lowest FWHM and therefore the best crystallinity over a range of energy from -10 V to – 40 V. The ideal case for epitaxial film growth is when a non-penetrating ion impacts the surface with enough energy to stimulate surface atom displacement/diffusion while minimizing that effect in the bulk [22-24] which makes heavy/large inert gasses like Kr ideal.

As shown below in MD simulations, gasses with small atomic radii like Ne can penetrate into the film and cause detrimental effects on crystallinity whereas Kr is much less prone to this while also being able to transfer large quantities of momentum at low energy owing to its large atomic mass. However, at very low bias energy, the use of Ne resulted in more effective crystallization than Ar. It is possible that this is due to the much higher ionization energy of Ne (21.6 eV) as compared to Ar (15.8 eV) and that at low kinetic energy, the potential energy imparted on the film as a result of neutralization of the Ne ions [22] (thermal energy of ~17.1 eV including AlN charge neutrality level of ~4.5 eV) [25] is the dominant effect whereas at higher kinetic energy (bias), momentum transfer induced collision cascades become the dominant factor. For low energy ions at -10 V, Ar ions do not have enough potential energy (compared to Ne ion) nor momentum transfer (compared to Kr), leading to poor crystallization of growing AlN films as shown in the left panel of Fig.4. 2.

AFM was used to verify the surface morphology of the films and as it can be seen in Fig. 4.3, all films were smooth, with sub-nm roughness that was nearly identical irrespective of the inert gas used for the ALA plasma treatment. The lack of damage from heavy ions is likely attributable to the low ion energies involved in the process as a result of the substrate biasing, which is a technique extensively used in PEALD to control ion energy and tailor material growth properties [26-27]. Therefore, it can be concluded at low energy, the potentially detrimental effects of ion bombardment by heavy gasses may be mitigated and that a heavy inert gas such as Kr may successfully be used for the ALA deposition of a smooth and highly crystalline film.

4.4.2 Effect of Plasma Delay Time on Atomic Layer Annealing

To further confirm the momentum transfer hypothesis, the effect of delay time between the ion treatment step and the TDMAA pulse was studied using Kr gas at -25 V stage bias. It has been previously reported that the delay between the ALA plasma treatment step and the following reactant pulse must be minimized to achieve the best crystallinity due to a surface heating effect; however, as seen in Fig. 4.4a, the crystallinity as determined by both signal intensity as well as FWHM of the AlN (002) peak is relatively unchanged from a 0 s delay to a 10 s delay. This is to be somewhat expected as many other previous reports on ion-irradiated solids have reported the "thermal spike" phase is usually on the order of 10^{-11}-10^{-12} s [22, 28] as opposed to the 10^{0} s timescales seen in other ALA reports using PEALD followed by inert gas ion treatment [7, 18, 29]. It is hypothesized that the apparent time dependence of crystallinity seen by others is due to partial surface

oxidation or some other form of surface contamination that occurs during the delay and interferes with crystallinity [30].

XPS was used to probe chemical composition of the two samples and as shown in Fig. 4.4b-c, XPS data of the samples with 0 s delay and 10 s delay have nearly identical, low O and C contamination and virtually identical chemical shift data that are consistent with the formation of AlN. Through the use of a high vacuum ALD system which included a liquid nitrogen cold trap to minimize background H_2O, film contamination was minimized even when using a 10 s delay and consistent with crystallinity being relatively unchanged irrespective of delay time, in agreement with the collision cascade hypothesis.

4.4.3 Effect of Intermittent Atomic Layer Annealing

As a final experimental verification of the idea of ion induced collision cascades, the ALA treatment was performed every cycle, every other cycle, and every third cycle. As it can be seen in Fig. 4.5, crystallinity rapidly fell off when dosing ions in every other cycle or every third cycle. This is consistent with ion induced crystallinity being confined to the first and second atomic layers and being extremely localized. If a heating effect on the order of 10^0 s was largely responsible for the crystallization effect, it is unlikely to be confined to only the first monolayer of the surface [31]; therefore, the data are much more consistent with the low energy incident ions transferring energy primarily to the top atomic layer of the growth surface which is then being dissipated via phonon transport in a short-lived process that acts as a localized thermal excitation.

4.4.4 Molecular Dynamics Simulations

To validate the experimental work and gain a deeper understanding of the ion-AlN interaction, classical molecular dynamics (MD) was used to investigate the ALA crystallization effect using Kr and Ne ions (the heaviest and lightest species tested experimentally). As shown schematically in Fig. 4.6a, the simulation involved a single inert gas atom with 40 eV energy colliding with an AlN structure composed of 1-2 monolayers of disordered AlN atop a perfectly crystalline AlN (002) slab. The disordered layer contained irregularities such as voids and two distinct types of defects that are shown schematically in Fig. 4.6b-c. The first defect was an interstitial Al point defect (hereafter referred to as defect 'A') and the second was a N point defect (hereafter referred to as defect 'B') that was part of a larger non-crystalline atomic chain.

Briefly summarizing the simulation details, the Vashishta potential [32] was used for AlN, and the interactions between inert gas atoms and AlN were described by the Lennard-Jones (LJ) potential. Parameter values for the LJ potential were determined using the Waldman-Hagler mixing rule [33]. To ensure simulations were accurate and realistic, the microcanonical ensemble was used with the timestep size selected to limit the displacement of an atom per step to 0.05 Å. All simulations were performed using LAMMPS [34] at an initial temperature of 0 K with visualizations generated using OVITO [35].

Based on the simulation results, two distinct interaction stages were found following the impact of an inert gas ion: the initial contact and final relaxation stages. During the initial contact stage, the incident ion quickly transfers its energy into the AlN over a period of ~0.1 ps (Fig. 4.7a) and although the timescale over which this energy

transfer occurred was similar for both Kr and Ne, qualitative and quantitative differences were noted. Whereas the Kr ion collision occurred as essentially a singular collision (owing to its higher momentum and/or larger atomic radius), the Ne atom underwent several sequential collisions (see non-monotonic decrease in energy for Ne in Fig. 4.7a), leading to a lower energy transfer per unit ion path length. This effect can be understood as stemming from the high elastic modulus of AlN (~500 GPa [36]), where a large force is needed to deform the surface. Because force is proportional to momentum, the higher mass Kr ion was able to deform the AlN surface and transfer a high amount of energy to a very localized area whereas the lighter Ne ion generated only a minor deformation before being deflected.

Although macroscopic energy transfer in the case of both Kr and Ne was similar, the use of Kr ions resulted in a more localized and more intense change in the potential and kinetic energy of the growing AlN film because unlike Ne atoms, Kr atoms did not undergo multiple, sequential collisions. This difference was quantified by comparing the local standard deviation of kinetic energy (σ_{KE}) and the local standard deviation of the change in potential energy of AlN ($\sigma_{\Delta PE}$) of AlN atoms nearby the impact site (Fig. 4.7b-c). The higher σ_{KE} measured in the case of Kr indicated more concentrated energy transfer to the AlN surface which could remove complex defects while the higher $\sigma_{\Delta PE}$ indicated the Kr ion generated a more localized and more intense heating effect.

In contrast to the fast initial contact stage, the relaxation stage occurs over longer timescales (several ps) corresponding to the "thermal spike" phase of ion-irradiated solids. It is during this stage that the local structure of AlN can be thermally relaxed using energy transferred from an impinging atom. In the cases of both Kr (Fig. 4.8a) and Ne (Fig. 4.8b),

defect 'A' is repaired during the relaxation stage as the defects received enough thermal energy to move into a crystalline site by surface heating; however, *defect 'B' was removed only in the case of Kr* because of the higher local energy required to remove the entire defect chain. Although the total amount of energy transferred is similar in the case of both Ne and Kr, the crystallization effect seen both experimentally and in simulations was seen to be stronger in the case of Kr, owing to the larger local momentum transfer of the Kr ion. It is also noted that owing to the larger atomic radius of Kr, the penetration depth of Kr is also much shallower as compared to Ne, which would reduce embedded species or the generation of defects in the bulk of the film.

The results of the simulation were in good agreement not only with the experimental data, but also with other ion-solid collision simulations modeling with the timescales over which the surface heating effect was expected to occur [22, 31]. Furthermore, the crystallization effect was shown both experimentally and in simulations of this work to depend on the inert gas used to bombard the growth surface: Kr is more effective than Ne due to higher energy transfer to the surface and lower penetration depth leading to effective defect healing in the crystallization of ALD grown amorphous layers on the bulk crystalline film.

4.5 Conclusion

In summary, it is demonstrated that the key mechanism of atomic layer annealing is a momentum transfer process where the incoming ions can remove defects both during the initial collision with the growing film and also during the later thermal relaxation stage where lattice vibrations act as local thermal excitation. Kr gas is shown experimentally to

result in higher crystallinity as measured via a smaller FWHM in GIXRD, and MD simulations confirm that Kr ions can repair a wider range of defects when compared to a lighter inert gas due to its larger and more localized momentum transfer to the growth surface. Furthermore, through the use of modest substrate biasing, it is shown that heavier ions (e.g., Kr) can successfully be used without introducing surface damage. By varying the time delay after ALA treatment together with XPS and GIXRD measurements, it is demonstrated that the local heating effect is extremely short lived and MD simulations are used to further reinforce this conclusion.

4.6 Acknowledgements

This work was supported in part by the Applications and Systems-Driven Center for Energy Efficient Integrated Nano Technologies (ASCENT), one of six centers in the Joint University Microelectronics Program (JUMP), an SRC program sponsored by the Defense Advanced Research Program Agency (DARPA). The authors would also like to gratefully acknowledge support from Applied Materials, Rasirc, and EMD.

Chapter 4, is in part or full, reprinted with permission from S. T. Ueda, A. McLeod, Y. Jo, J. Spiegelman, J. Spiegelman, D. Alvarez, D. Moser, R. Kanjolia, M. Moinpour, J. Woodruff, K. Cho, and A. C. Kummel, "Experimental and Theoretical Determination of the Role of Ions in Atomic Layer Annealing", *manuscript submitted to Journal of Materials Chemistry C*. The dissertation/thesis author was the primary investigator and author of this paper.

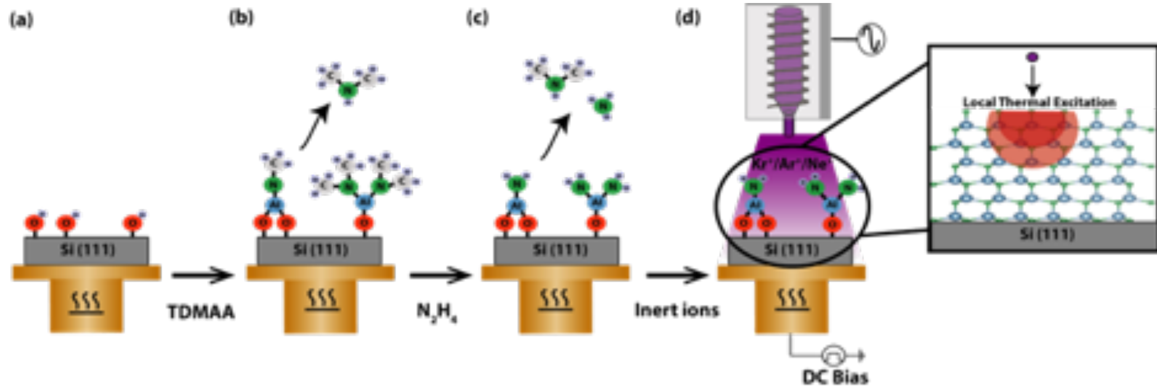

Figure 4.1. Schematic Diagram of the ALA AlN Process. (a) Using hydroxyl-terminated Si as the starting substrate, (b) tris(dimethylamido) aluminum (TDMAA) dosing results in a surface terminated in aluminum dimethylamide and the release of dimethylamine gas. (c) Hydrazine (N_2H_4) dosing removes the surface bound dimethylamide as dimethylamine and ammonia gas. (d) The final step in the ALA process consists of low energy inert ion bombardment which induces crystallinity via a momentum transfer process that generates local thermal excitation (inset).

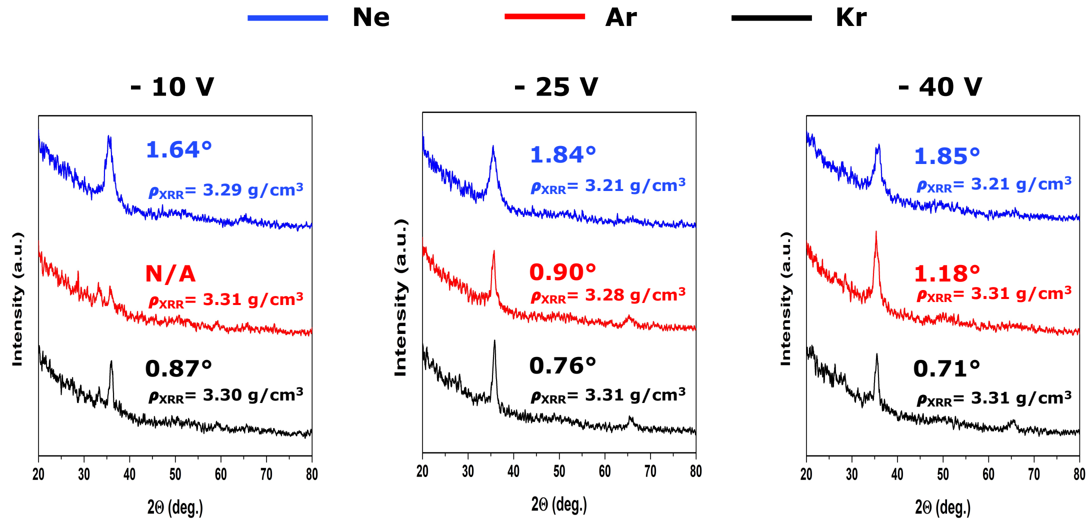

Figure 4.2. GIXRD data comparing ALA AlN films using Ne, Ar, or Kr gas at various bias voltages. Using the FWHM of the AlN (002) peak as a metric for crystallinity, Kr can be seen to result in the highest quality crystalline films over a wide range in energy. At -25 V and -40 V bias, crystallinity can be seen to scale with ion mass consistent with the momentum transfer hypothesis. Note: Treatment time for all samples was fixed at 20 s while ion current density was maintained at a constant ~0.25 mA/cm^2 (~1.5*10^{19} ions m^{-2} s^{-1}) for all conditions. All samples were approximately the same thickness of ~40 nm as measured by XRR. All samples had near bulk density consistent with a very low fraction of amorphous material.

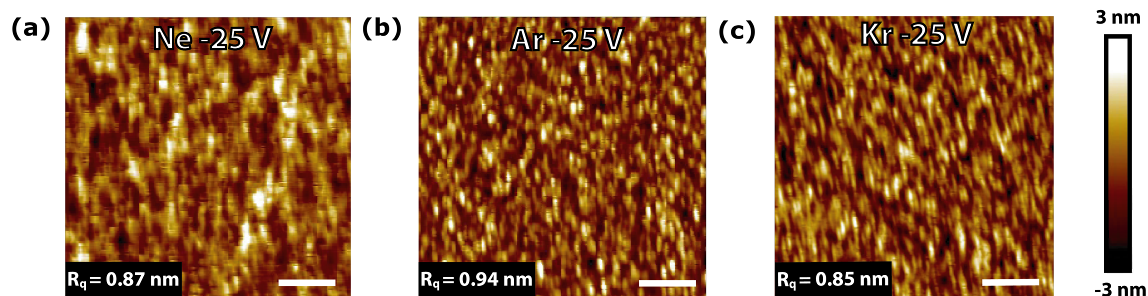

Figure 4.3. AFM data comparing effect inert gas used during ALA. At a constant bias of -25 V, AFM data show RMS surface roughness (R_q) is relatively unchanged when using (a) Ne, (b) Ar, or (c) Kr as the gas in the ALA process with all cases displaying sub-nm roughness. Scale bar, 500 nm.

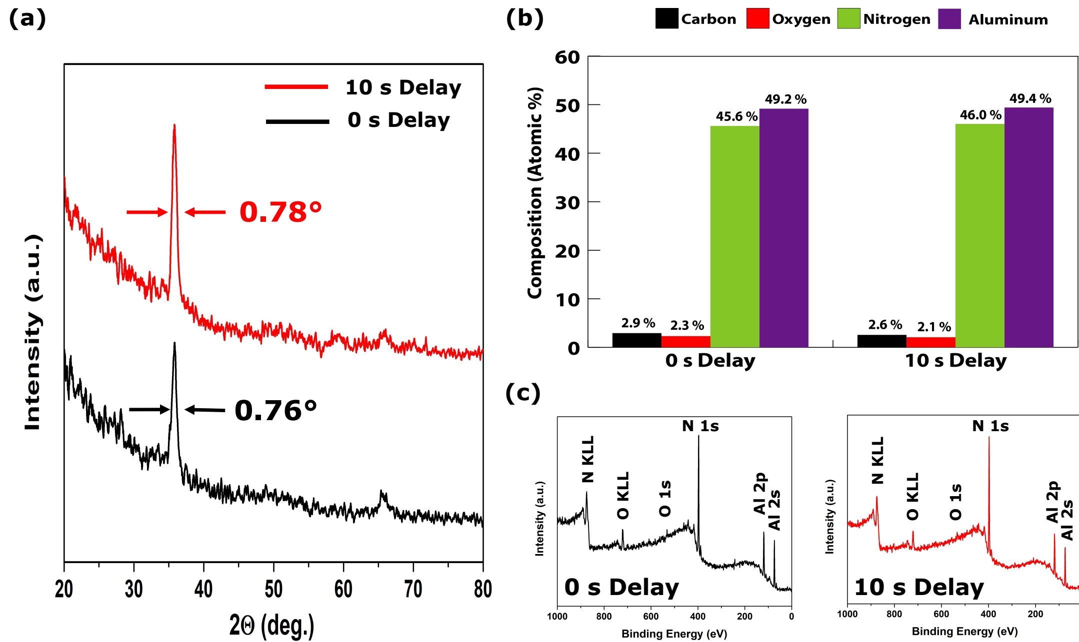

Figure 4.4. GIXRD and XPS comparing effect of ALA delay time on crystallinity. (a) As compared to using a 0 s delay (instant) between the ALA plasma treatment step and the subsequent organometallic pulse, using a delay of 10 s results in no reduction in AlN crystalline quality in GIXRD as measured by both signal intensity as well as FWHM. (b-c) XPS chemical composition data are nearly identical for 0 s and 10 s delay.

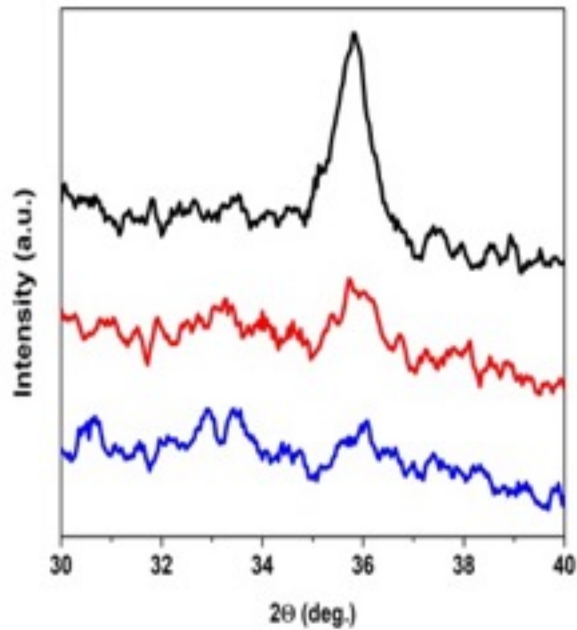

Figure 4.5. GIXRD data comparing effect of cycles per ALA treatment. Crystallinity is seen to rapidly decrease as a function of cycles per ALA treatment. When performed every cycle, crystallinity is strong (black), while the AlN (002) peak is barely above signal-to-noise when performing ALA every other cycle (red). Performing ALA every third cycle results in no detectable crystallinity (blue).

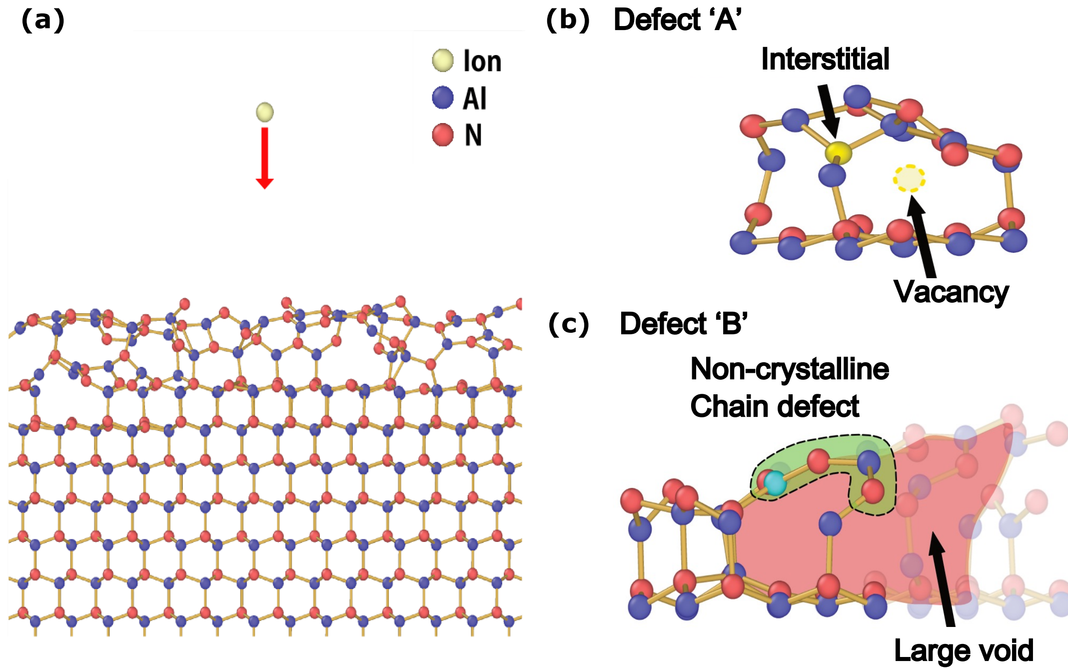

Figure 4.6. Schematic diagram of ion impact simulation. (a) The simulation consisted of a single 40 eV inert gas ion colliding with an AlN surface comprised of a disordered layer atop a crystalline AlN (002) slab. The disordered layer contains voids and defects to simulate the AlN film before ALA treatment. (b) The first defect included in the simulation (defect 'A') is a Frenkel defect generated by an interstitial Al atom (yellow). The interstitial generated an Al vacancy depicted as a hollow yellow circle. (c) The second defect in the simulation (defect 'B') is a larger, non-crystalline atomic chain defect shown representatively as a N point defect (turquoise) for ease of viewing. The point defect is just one of the atoms in a non-crystalline position.

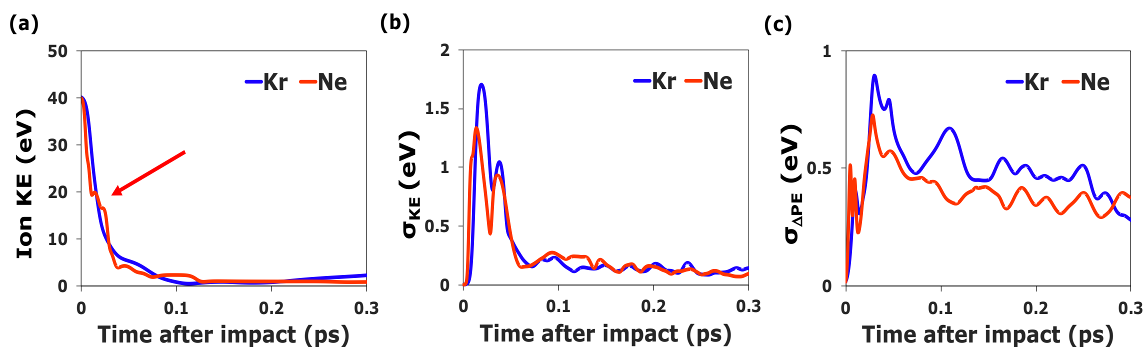

Figure 4.7. Simulation results during initial contact phase of ion collision. (a) During initial contact with AlN, both Kr (blue) and Ne (red) show similar kinetic energy profiles which show the transfer of energy to AlN occurred over a timescale of ~0.1 ps; however, a non-monotonic decrease in Ne kinetic energy was seen due to the atom undergoing multiple sequential collisions (b) The local standard deviation of kinetic energy (σ_{KE}) of AlN atoms nearby the impact site is greater in the first collision (peak at ~0.01 ps) in the case of Kr because the Kr has a higher energy loss per unit length, leading to a more intense and more localized energy transfer to AlN. (c) The standard deviation of the change in potential energy of AlN ($\sigma_{\Delta PE}$) is greater in the case of Kr due to the multiple, sequential collisions generated by Ne generating a more diffuse surface heating as compared to the singular impact in the case of Kr.

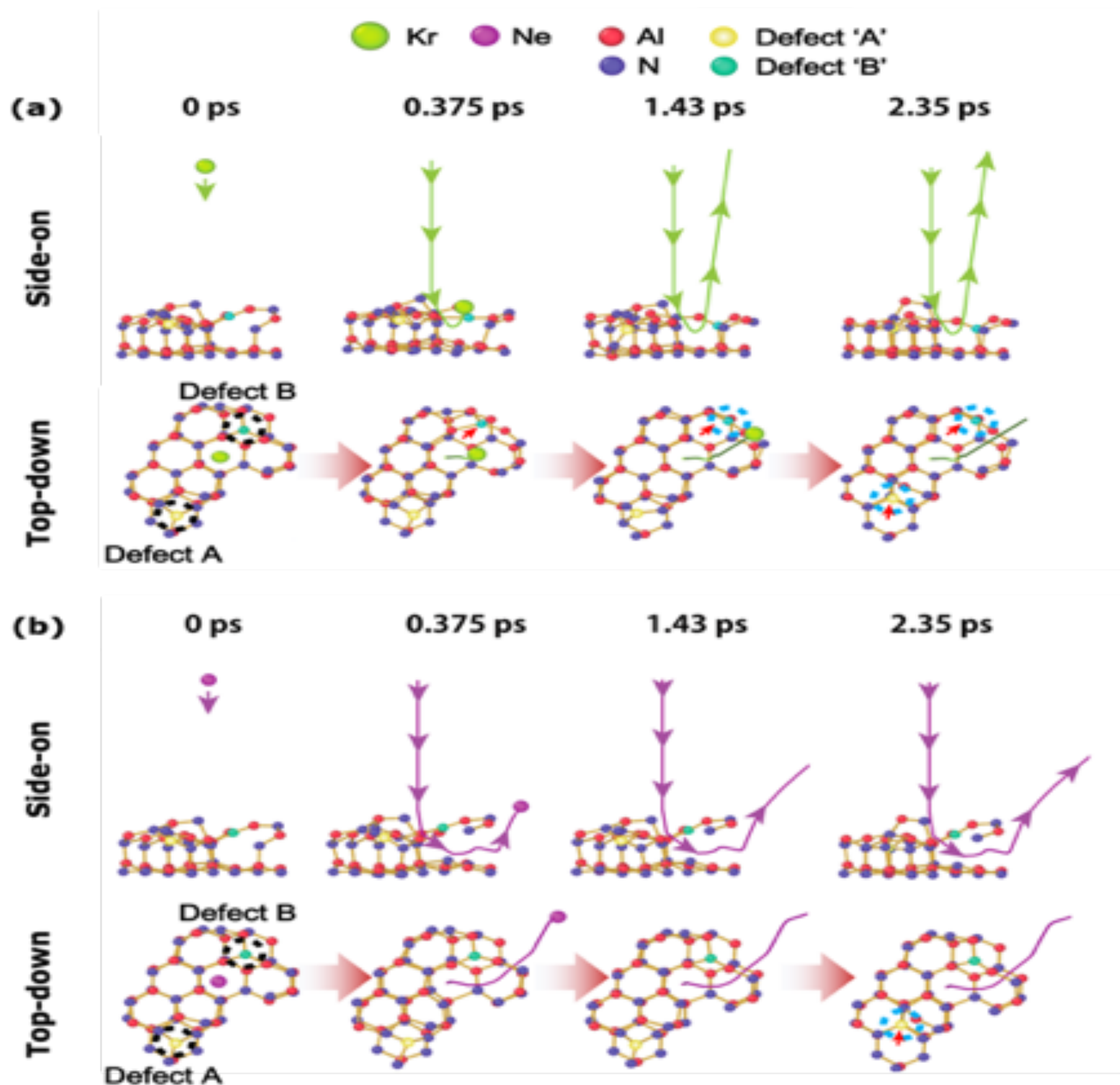

Figure 4.8. MD simulation of the local structure relaxation of AlN with an impinging atom. Atoms are color-coded with respect to atomic species except for the two defects. The solid lines are the trajectories of the impinging inert gas atoms. Defects are circled in cyan if they are repaired during the collision cascade. (a) The Kr ion is shown to not penetrate into the bulk of the film and results in the annihilation of defect 'B' within < 1 ps of ion impact and the repair of defect 'A' after several ps (b) The Ne ion is shown to penetrate further into the AlN film while also being unable to repair or remove defect 'B' though the surface heating effect was still able to remove defect 'A' after ~ 2 ps. The full collision simulation is shown in supplementary video 1 and 2.

4.7 References

[1] Ferain, I.; Colinge, C. A.; Colinge, J. P. Multigate Transistors as the Future of Classical Metal-Oxide-Semiconductor Field-Effect Transistors. *Nature*. 2011. https://doi.org/10.1038/nature10676.

[2] Fang, M.; Ho, J. C. Area-Selective Atomic Layer Deposition: Conformal Coating, Subnanometer Thickness Control, and Smart Positioning. *ACS Nano*. 2015. https://doi.org/10.1021/acsnano.5b05249.

[3] Leskelä, M.; Ritala, M. Atomic Layer Deposition Chemistry: Recent Developments and Future Challenges. *Angewandte Chemie - International Edition*. 2003. https://doi.org/10.1002/anie.200301652.

[4] Johnson, R. W.; Hultqvist, A.; Bent, S. F. A Brief Review of Atomic Layer Deposition: From Fundamentals to Applications. *Materials Today*. 2014. https://doi.org/10.1016/j.mattod.2014.04.026.

[5] Oviroh, P. O.; Akbarzadeh, R.; Pan, D.; Coetzee, R. A. M.; Jen, T. C. New Development of Atomic Layer Deposition: Processes, Methods and Applications. *Science and Technology of Advanced Materials*. 2019. https://doi.org/10.1080/14686996.2019.1599694.

[6] Ovanesyan, R. A.; Filatova, E. A.; Elliott, S. D.; Hausmann, D. M.; Smith, D. C.; Agarwal, S. Atomic Layer Deposition of Silicon-Based Dielectrics for Semiconductor Manufacturing: Current Status and Future Outlook. *J. Vac. Sci. Technol. A* **2019**. https://doi.org/10.1116/1.5113631.

[7] Shih, H. Y.; Lee, W. H.; Kao, W. C.; Chuang, Y. C.; Lin, R. M.; Lin, H. C.; Shiojiri, M.; Chen, M. J. Low-Temperature Atomic Layer Epitaxy of AlN Ultrathin Films by Layer-by-Layer, in-Situ Atomic Layer Annealing. *Sci. Rep.* **2017**. https://doi.org/10.1038/srep39717.

[8] Clement, M.; Vergara, L.; Sangrador, J.; Iborra, E.; Sanz-Hervás, A. SAW Characteristics of AlN Films Sputtered on Silicon Substrates. In *Ultrasonics*; 2004. https://doi.org/10.1016/j.ultras.2004.01.034.

[9] Loebl, H. P.; Klee, M.; Metzmacher, C.; Brand, W.; Milsom, R.; Lok, P. Piezoelectric Thin AlN Films for Bulk Acoustic Wave (BAW) Resonators. *Mater. Chem. Phys.* **2003**. https://doi.org/10.1016/S0254-0584(02)00252-3.

[10] Umeda, K.; Kawamura, H.; Takeuchi, M.; Yoshino, Y. Characteristics of an AlN-Based Bulk Acoustic Wave Resonator in the Super High Frequency Range. *Vacuum* **2008**. https://doi.org/10.1016/j.vacuum.2008.04.044.

[11] Gillinger, M.; Shaposhnikov, K.; Knobloch, T.; Stöger-Pollach, M.; Artner, W.; Hradil, K.; Schneider, M.; Kaltenbacher, M.; Schmid, U. Enhanced C-Axis Orientation of Aluminum Nitride Thin Films by Plasma-Based Pre-Conditioning of Sapphire Substrates for SAW Applications. *Appl. Surf. Sci.* **2018**. https://doi.org/10.1016/j.apsusc.2017.11.113.

[12] Xu, R. L.; Munõz Rojo, M.; Islam, S. M.; Sood, A.; Vareskic, B.; Katre, A.; Mingo, N.; Goodson, K. E.; Xing, H. G.; Jena, D.; et al. Thermal Conductivity of Crystalline AlN and the Influence of Atomic-Scale Defects. *J. Appl. Phys.* **2019**. https://doi.org/10.1063/1.5097172.

[13] Duquenne, C.; Besland, M. P.; Tessier, P. Y.; Gautron, E.; Scudeller, Y.; Averty, D. Thermal Conductivity of Aluminium Nitride Thin Films Prepared by Reactive Magnetron Sputtering. *J. Phys. D. Appl. Phys.* **2012**. https://doi.org/10.1088/0022-3727/45/1/015301.

[14] Bian, Y.; Liu, M.; Ke, G.; Chen, Y.; DiBattista, J.; Chan, E.; Yang, Y. Aluminum Nitride Thin Film Growth and Applications for Heat Dissipation. *Surf. Coatings Technol.* **2015**. https://doi.org/10.1016/j.surfcoat.2014.11.060.

[15] Yi, S. H.; Huang, K. W.; Lin, H. C.; Chen, M. J. Low-Temperature Crystallization and Paraelectric-Ferroelectric Phase Transformation in Nanoscale ZrO2 Thin Films Induced by Atomic Layer Plasma Treatment. *J. Mater. Chem. C* **2020**. https://doi.org/10.1039/c9tc04801d.

[16] Kao, W. C.; Lee, W. H.; Yi, S. H.; Shen, T. H.; Lin, H. C.; Chen, M. J. AlN Epitaxy on SiC by Low-Temperature Atomic Layer Deposition: Via Layer-by-Layer, in Situ Atomic Layer Annealing. *RSC Adv.* **2019**. https://doi.org/10.1039/c9ra00008a.

[17] Seppänen, H.; Kim, I.; Etula, J.; Ubyivovk, E.; Bouravleuv, A.; Lipsanen, H. Aluminum Nitride Transition Layer for Power Electronics Applications Grown by Plasma-Enhanced Atomic Layer Deposition. *Materials (Basel).* **2019**. https://doi.org/10.3390/ma12030406.

[18] Lee, W. H.; Yin, Y. T.; Cheng, P. H.; Shyue, J. J.; Shiojiri, M.; Lin, H. C.; Chen, M. J. Nanoscale GaN Epilayer Grown by Atomic Layer Annealing and Epitaxy at Low Temperature. *ACS Sustain. Chem. Eng.* **2019**. https://doi.org/10.1021/acssuschemeng.8b03982.

[19] Ueda, S. T.; McLeod, A.; Alvarez, D.; Moser, D.; Kanjolia, R.; Moinpour, M.; Woodruff, J.; Kummel, A. C. Tris(Dimethylamido)Aluminum(III) and N2H4: Ideal Precursors for the Low-Temperature Deposition of Large Grain, Oriented c-Axis AlN on Si via Atomic Layer Annealing. *Appl. Surf. Sci.* **2021**. https://doi.org/10.1016/j.apsusc.2021.149656.

[20] Cao, X. A.; Pearton, S. J.; Zhang, A. P.; Dang, G. T.; Ren, F.; Shul, R. J.; Zhang, L.; Hickman, R.; Van Hove, J. M. Electrical Effects of Plasma Damage in P-GaN. *Appl. Phys. Lett.* **1999**. https://doi.org/10.1063/1.125080.

[21] Holgado, J. P.; Barranco, A.; Yubero, F.; Espinos, J. P.; González-Elipe, A. R. Ion Beam Effects in SiOx (x < 2) Subjected to Low Energy Ar+, He+ and N2+ Bombardment. *Nucl. Instruments Methods Phys. Res. Sect. B Beam Interact. with Mater. Atoms* **2002**. https://doi.org/10.1016/S0168-583X(01)01153-3.

[22] Anders, A. A Structure Zone Diagram Including Plasma-Based Deposition and Ion Etching. *Thin Solid Films* **2010**. https://doi.org/10.1016/j.tsf.2009.10.145.

[23] Brice, D. K.; Tsao, J. Y.; Picraux, S. T. Partitioning of Ion-Induced Surface and Bulk Displacements. *Nucl. Inst. Methods Phys. Res. B* **1989**. https://doi.org/10.1016/0168-583X(89)90690-3.

[24] Carter, G. Influence of Thermal Spikes on Preferred Grain Orientation in Ion-Assisted Deposition. *Phys. Rev. B - Condens. Matter Mater. Phys.* **2000**. https://doi.org/10.1103/PhysRevB.62.8376.

[25] Brudnyi, V. N. BN, AIN, GaN, InN: Charge Neutrality Level, Surface, Interfaces, Doping. *Russ. Phys. J.* **2017**. https://doi.org/10.1007/s11182-017-1035-5.

[26] Profijt, H. B.; Van De Sanden, M. C. M.; Kessels, W. M. M. Substrate Biasing during Plasma-Assisted ALD for Crystalline Phase-Control of TiO 2 Thin Films. *Electrochem. Solid-State Lett.* **2012**. https://doi.org/10.1149/2.024202esl.

[27] Profijt, H. B.; van de Sanden, M. C. M.; Kessels, W. M. M. Substrate-Biasing during Plasma-Assisted Atomic Layer Deposition to Tailor Metal-Oxide Thin Film Growth. *J. Vac. Sci. Technol. A Vacuum, Surfaces, Film.* **2013**. https://doi.org/10.1116/1.4756906.

[28] Liu, J. C.; Li, J.; Mayer, J. W. Temperature Effect on Ion-Irradiation-Induced Grain Growth in Cu Thin Films. *J. Appl. Phys.* **1990**. https://doi.org/10.1063/1.345530.

[29] Lee, W. H.; Kao, W. C.; Yin, Y. T.; Yi, S. H.; Huang, K. W.; Lin, H. C.; Chen, M. J. Sub-Nanometer Heating Depth of Atomic Layer Annealing. *Appl. Surf. Sci.* **2020**. https://doi.org/10.1016/j.apsusc.2020.146615.

[30] Brien, V.; Pigeat, P. Correlation between the Oxygen Content and the Morphology of AlN Films Grown by r.f. Magnetron Sputtering. *J. Cryst. Growth* **2008**. https://doi.org/10.1016/j.jcrysgro.2008.06.021.

[31] Atwater, H. A.; Thompson, C. V.; Smith, H. I. Ion-Bombardment-Enhanced Grain Growth in Germanium, Silicon, and Gold Thin Films. *J. Appl. Phys.* **1988**. https://doi.org/10.1063/1.341665.

[32] Vashishta, P.; Kalia, R. K.; Nakano, A.; Rino, J. P. Interaction Potential for Aluminum Nitride: A Molecular Dynamics Study of Mechanical and Thermal Properties of Crystalline and Amorphous Aluminum Nitride. *J. Appl. Phys.* **2011**. https://doi.org/10.1063/1.3525983.

[33] Waldman, M.; Hagler, A. T. New Combining Rules for Rare Gas van Der Waals Parameters. *J. Comput. Chem.* **1993**. https://doi.org/10.1002/jcc.540140909.

[34] Plimpton, S. Fast Parallel Algorithms for Short-Range Molecular Dynamics. *J. Comput. Phys.* **1995**. https://doi.org/10.1006/jcph.1995.1039.

[35] Stukowski, A. Visualization and Analysis of Atomistic Simulation Data with OVITO-the Open Visualization Tool. *Model. Simul. Mater. Sci. Eng.* **2010**. https://doi.org/10.1088/0965-0393/18/1/015012.

[36] Lu, Y.; Reusch, M.; Kurz, N.; Ding, A.; Christoph, T.; Prescher, M.; Kirste, L.; Ambacher, O.; Žukauskaitė, A. Elastic Modulus and Coefficient of Thermal Expansion of Piezoelectric Al1−xScxN (up to x = 0.41) Thin Films. *APL Mater.* **2018**. https://doi.org/10.1063/1.5040190.